

# A Rho-GTPase based model explains group advantage in collective chemotaxis of neural crest cells

Brian Merchant<sup>1</sup> and James J. Feng<sup>1,2\*</sup>

<sup>1</sup> Department of Mathematics, University of British Columbia, Vancouver, BC V6T 1Z2, Canada

<sup>2</sup> Department of Chemical and Biological Engineering, University of British Columbia, Vancouver, BC V6T 1Z3, Canada

(January 25, 2020)

## Abstract

A cluster of neural crest cells may chemotax up a shallow external gradient to which a single cell is unresponsive. To explain this intriguing “group advantage”, we propose a chemo-mechanical model based on the signaling proteins Rac1 and RhoA. We represent each cell as a polygon with nodes connected by elastic membranes. Via reaction-diffusion on the membrane and exchange with their cytosolic pools, Rac1 and RhoA interact to produce cell polarization and repolarization subject to random noise. Mechanically, we represent cell motility via overdamped nodal motion subject to passive elastic membrane forces and active protrusive or contractile forces where Rac1 or RhoA dominates. The model reproduces the random walk of a single cell in a weak gradient and two modes of cell-cell interaction: contact inhibition of locomotion and co-attraction. The simultaneous action of contact inhibition and co-attraction suppresses random Rac1 bursts on the membrane and serves to preserve existing protrusions. This amounts to an emergent persistence of polarity that markedly enhances the ability of a cluster of neural crest cells to chemotax in a weak gradient against random noise, thereby giving rise to the group advantage.

---

\*Corresponding author. E-mail: james.feng@ubc.ca

**Keywords:** contact inhibition of locomotion, co-attraction, persistence of polarity, Rac1, RhoA, gradient sensing, collective migration

## 1 Introduction

Chemotaxis is central to many developmental, physiological and pathological processes such as embryogenesis, wound healing, the immune response and cancer metastasis. It has been studied extensively in recent decades, but many mysteries remain. One remarkable phenomenon is “group advantage” in chemotaxis: a group of cells may chemotax successfully up a gradient in the chemoattractant concentration that is too shallow for a single cell to detect or follow [1,2]. For example, *in vitro* observations of clusters of highly motile neural crest cells (NCCs) exhibit directional movement towards a bead soaked in the chemoattractant CXCL12 (Sdf1), while a single NCC fails to chemotax, wandering instead along a tortuous trajectory that resembles random walk [3]. T and B lymphocytes show similar group advantage in finely controlled chemoattractant gradients of CXCL12 and CCL19 [4], as do mammary epithelial cells in response to EGF [5]. The ability to sense weak gradients, arising from inter-cellular dynamics within a cluster, has been aptly called “emergent gradient sensing” [2].

A variety of mechanisms have been proposed to explain the group advantage, and a recent review brings some conceptual clarity by categorizing the proposed mechanisms into 5 classes, ranging from simple *null models* that posit cell-cell contact as the direct trigger for gradient sensing to more sophisticated schemes of tug-of-war or relay of locally generated gradients [2]. Although insightful, all this modeling is phenomenological at heart. It starts from the standpoint of the final outcome, and asks what potential physical mechanisms could, in proper combination, have produced the observed outcome. As such, these models do not focus on the biological mechanisms that have enabled the process. From this argument, we feel that a more mechanistic type of modeling can be useful. It will provide a more direct linkage to biological understanding of signaling pathways, and perhaps will be better able to suggest experiments for testing the model hypotheses.

Toward such mechanistic modeling, we seek clues from the experimental observations. In the literature on neural crest cells, which are among the most extensively studied cell types in the context of collective chemotaxis, two such clues stand out: contact inhibition of locomotion (CIL)

and co-attraction (COA). Theveneau *et al.* [3] discovered that cluster response to a weak gradient could be suppressed by inhibiting expression of the adhesion molecule N-cadherin on the cell surface. N-cadherin is a key player in CIL. When two cells come into contact, N-cadherin mediates the down-regulation of Rac1 and the up-regulation of RhoA in the protrusion fronts in contact. Thus the protrusion fronts are turned into contractile rears, and the two cells repolarize and move away from each other. When CIL is disabled in NCCs by inhibiting expression of N-cadherin, the cells clump into a dense cluster that fails to chemotax up a shallow gradient of Sdf1. The second clue is co-attraction among NCCs mediated by the C3a-C3aR binding [6]. NCCs release the ligand C3a into the surrounding ECM while expressing its receptor C3aR on the membrane. The C3a-C3aR binding up-regulates Rac1 and promotes protrusion toward the nearest neighbors, thus encouraging clustering of NCCs. Carmona-Fontaine *et al.* [6] found that inhibiting COA by introducing either C3a or C3aR deficiency caused a cluster to scatter, and to lose its group advantage in collective chemotaxis.

Based on the experimental evidence briefly summarized above, we hypothesize that cell-cell interaction under the simultaneous influence of CIL and COA inhibits the random repolarization of NCCs that would normally dominate the behavior of an isolated cell. This will give rise to a persistence in polarity (POP) for a cluster of cranial NCCs, which as a result chemotaxes up a gradient in chemoattractant that would have been too shallow to induce chemotaxis of a single NCC. In the following we build a mathematical model to test this hypothesis for the group advantage in cranial NCCs.

## 2 Methods

Since CIL and COA are both rooted in the activity of the Rho-family of GTPases [3,6] that underlie the polarization of a single cell [7,8], we base our model on the known signaling pathways of Rac1 and RhoA. Previously, we have developed a GTPase-based biomechanics model to demonstrate how CIL and COA interact to produce POP in NCC clusters so that they spontaneously migrate down a confined channel without chemoattractant [9]. This model will be extended by endowing the model cells with a gradient-sensing capability and by adding a shallow, linear chemoattractant gradient.

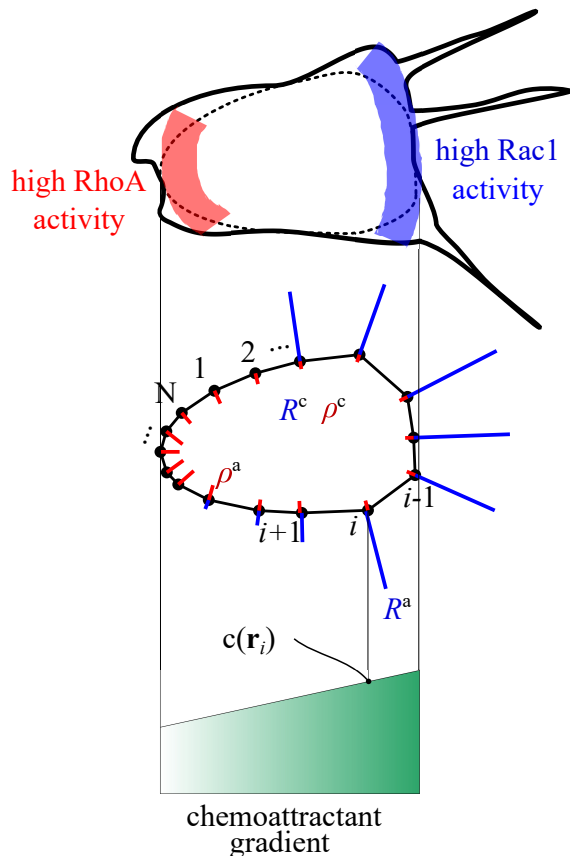


Figure 1: A model cell represented by a polygon of  $N$  nodes connected by elastic edges. The nodes bear active and inactive levels of Rac1 ( $R^a$  and  $R^i$ , respectively), with  $R^a$  represented by blue line segments pointing outward. Similarly, active and inactive RhoA ( $\rho^a$  and  $\rho^i$ , respectively) are defined on each node, with  $\rho^a$  represented by red line segments pointing inward. The cytosolic Rac1 ( $R^c$ ) and RhoA ( $\rho^c$ ) are each well mixed. Each node senses the level  $c(\mathbf{r})$  of a prescribed linear chemoattractant gradient.

We represent each cell by a two-dimensional polygon with nodes connected by elastic edges (Fig. 1). On the nodes we define active and inactive forms of Rac1 and RhoA, and the movement of the nodes subject to active and passive forces determines cell motility. Our model has a biochemical component and a mechanical component. The biochemical model starts with known pathways of Rac1 and RhoA—their autoactivation and mutual inhibition—and ends with the production of cell polarization. We also introduce a noise that periodically promotes Rac1 activity on randomly selected nodes with the potential to outcompete existing protrusion fronts to produce repolarization. Finally, we have added gradient sensing to the model by encouraging Rac1 activity based on an intracellular measurement of a chemoattractant gradient. As demonstrated earlier [9], our GTPase-based model captures CIL and COA, respectively, by allowing mechanical contact and C3a sensing

to modulate the Rac-Rho dynamics. Mechanically, we compute a protrusive or contractile active force on each node depending on whether the active Rac1 or RhoA dominates on the node. Besides, the node also experiences elastic forces from the edges and a pressure from the cytosol. The total force on each node determines its motion by overdamped dynamics, thereby realizing cell deformation and movement. Since the bulk of the model is similar to that of Merchant *et al.* [9], we have relegated a detailed description to the online Supplemental Information (SI). In the following we highlight a few key features.

The model tracks three forms of Rac1 and RhoA: active and membrane-bound, inactive and membrane-bound, and inactive within the cytosol. The total amount of each Rho GTPase in all three forms is conserved. We assume that the cytosol is well-mixed, owing to the rapid diffusivity of Rho GTPases through the cytosol as compared to along the membrane [10–12]. Cell polarization will arise from the reaction-diffusion of the GTPases on the membrane and their exchange with the cytosol, and will be manifested by spatially segregated groups of vertices exhibiting either high levels of Rac1 activity or high levels of RhoA activity. For example, the evolution of the active Rac1 ( $R^a$ ) on node  $i$  is governed by

$$\frac{dR_i^a}{dt} = K^+ R_i^i - K^- R_i^a + (J_{i-1}^a - J_i^a), \quad (1)$$

where  $K^\pm$  are the activation and deactivation rates and  $R^i$  is the local concentration of the inactive Rac1.  $J_i^a$  is the diffusive flux of  $R^a$  from node  $i$  to  $i + 1$ .

The key factors of the model, polarization, random repolarization, CIL, COA, and gradient sensing, are all encoded in the kinetic rates  $K^\pm$  and similar rates  $\kappa^\pm$  for RhoA. As an illustration, the Rac1 activation rate

$$K^+(i, t) = [x_r(i, t) + x_a(i, t)]K_b^+ + H(R_i^a)K_A^+(1 + C_i) \quad (2)$$

contains a baseline activation rate  $K_b^+$ , multiplied by the randomization factor  $x_r$  and co-attraction factor  $x_a$ , and an autoactivation rate  $K_A^+$ , multiplied by a Hill function  $H$  and, importantly, a chemoattractant sensing factor  $(1 + C_i)$ . Having the chemoattractant act on the autoactivation term, as opposed to the baseline term, is motivated by experimental observations that Sdf1 does

not elevate Rac1 generally on the cell membrane but only strengthens existing protrusions [3]. Moreover, as our model accounts for co-attraction by summing up signaling from all cells, the  $x_a$  factor would be greater for larger clusters, and thus needs to be normalized to maintain roughly the same average cell-cell separation. This and other algebraic details are given in the SI. Note that we introduce random noise into the kinetics through  $x_r$  acting on the baseline Rac1 activation. This is therefore an internal noise unrelated to any external gradient or gradient sensing mechanism. This differs from the typical treatment of noise in existing models, where it enters either through gradient measurement or directly into the cell's equation of motion. For this reason, our model cannot be easily classified into any of the modeling paradigms reviewed by Camley [2].

The treatment of the gradient-sensing factor  $C$  is important in the current context, but little is known of the sensing mechanism employed by neural crest cells. The question of whether they sense the local concentration or the gradient is not completely settled, although recent evidence suggests that NCCs appear to sense the gradient [2, 13]. For lack of a detailed mechanism for gradient sensing, we will not account for the kinetics of binding and unbinding as considered by Camley [2], but adopt a simple model that measures the difference in the chemoattractant concentration across the cell.

We ignore any local modification of the chemoattractant by the cells, and assume that the nodes on a cell sense the chemoattractant according to a prescribed spatial profile. We impose a radially linear profile for the concentration of the chemoattractant with a cut-off distance of  $50d$ ,  $d$  being the cell diameter:

$$c(\mathbf{r}) = \begin{cases} M(1 - \frac{|\mathbf{r}|}{50d}), & |\mathbf{r}| \leq 50d \\ 0, & |\mathbf{r}| > 50d \end{cases} \quad (3)$$

where  $\mathbf{r}$  is the position vector and the maximum concentration  $M$  occurs at the origin  $\mathbf{r} = 0$ . To calculate the gradient sensing factor  $C_i$  at node  $i$  on a cell, we find the node  $j$  on the same cell that is farthest from the source and hence senses the lowest level of  $c$ , and then take the difference

$$C_i = c(\mathbf{r}_i) - c(\mathbf{r}_j) \quad (4)$$

to be the gradient sensing factor in Eq. (2). This ensures that the GTPases react not to the local concentration  $c$  but to its spatial gradient. Note that we have little quantitative knowledge on how

the chemoattractant gradient affects the kinetic rates. Therefore, we have taken  $C$ ,  $c$  and  $M$  to be dimensionless for mathematical simplicity.

Altogether, the model has more than 20 geometric, physical and kinetic parameters. Most of these can be estimated, at least approximately, from experimental data or from prior modeling. In the SI we tabulate these estimations together with the relevant sources. This set of parameters form the basis for parametric studies, and will be called the “standard parameter set” hereafter.

### 3 Results

In setting up our *in silico* chemotaxis assay, we pose the concentration field of Eq. (3) centered at the origin  $\mathbf{r} = 0$ , and put a single cell or a cluster of cells at an initial distance of  $D_0 = 625 \mu\text{m}$  from the origin, the cell diameter being  $d = 40 \mu\text{m}$ . For a single cell, the initial distance  $D_0$  is measured from its center. A cluster has a closely packed square shape initially, and  $D_0$  is from the center of the cell closest to the origin. The initial configuration of the cluster, as long as the cells are in close proximity, has little effect on the subsequent dynamics. The cells have zero initial velocity, and are assigned randomized initial Rac1 and RhoA profiles on their membrane, with the active, inactive and cytosolic forms of each Rho GTPase being 10%, 10% and 80% of its total amount. Upon start of the simulation, the GTPases evolve according to the kinetic equations, yielding cell polarization and protrusion from a wave-pinning mechanism [10, 14]. Depending on the magnitude of the gradient  $M$  (see Eq. 3), cell motion may be dominated either by chemotaxis or by the random repolarization within the Rho-GTPase dynamical system (through the  $x_r$  term in Eq. 2). The focus of this study is on shallow gradients that a single cell cannot follow persistently in chemotaxis, but a cluster can.

To measure the success of chemotaxis, we define a circular “target zone” of radius  $4d$  at the origin. If a node of one of the cells from a cluster enters the target zone within a period of 10 hours, this is counted as a successful chemotaxis. Then a success rate  $S$  can be computed as the percentage of successful runs after many (typically 20) repeated realizations of the chemotactic simulation. Note that  $S$  is not a rigorous and universal measurement of chemotactic success, and is subject to limitations. The target zone and time period are both prescribed *ad hoc*, so the absolute value of the success rate is not meaningful. Besides, it is intended for a *cohesive* cluster. Under

impaired COA, a cluster may scatter with one or more of the cells wandering into the target zone (cf. Sec. 3.4C). Such a scenario should not be counted as successful collective chemotaxis. Subject to the above caveats,  $S$  serves as a convenient index for quantifying the group advantage of collective chemotaxis relative to that of a single cell.

To understand the phenomenon of group advantage in chemotaxis, we will first study the motion of solitary cells and cell clusters in the absence of a chemoattractant. This comparison will afford us the opportunity to elucidate how the simultaneous action of CIL and COA suppresses random repolarization to produce POP. Then we examine single cells and cell clusters in a shallow gradient, and demonstrate how POP gives rise to the group advantage.

### 3.1 Solitary cell motility in the absence of a chemoattractant

*Xenopus* cranial neural crest cells alternate between phases of persistent movement and low-persistence movement due to repolarization events; this pattern has been called “run-and-tumble” in the literature [3]. Cell speeds were measured at about  $3 \mu\text{m}/\text{min}$  during the persistent “run” phase [15, 16]. This has been used to tune the mechanical parameters (especially the friction factor  $\eta$  and the active force factors  $K_R$  and  $K_\rho$  as explained in Sec. 2 of the SI) in the model so as to reproduce the correct run speed. Similarly, because the persistent movement typically lasts around 20 minutes, the interval between random bursts in Rac1 activity is chosen according to a normal distribution so as to produce a single-cell persistence time consistent with experimental observations.

Using the standard set of parameters, the single-cell behavior in the absence of a chemoattractant is essentially the same as reported in Merchant *et al.* [9]. Movie S1 in the SI shows a representative run, and Fig. 2(a) plots the trajectories of 20 repeated runs. A more detailed discussion of the single-cell dynamics can be found in the earlier study [9].

### 3.2 Group behavior in the absence of a chemoattractant

Merchant *et al.* [9] have shown that their GTPase-based model was able to recapitulate the two key factors in cell-cell interaction: CIL and COA. These features have carried over to our extended model. The simultaneous action of CIL and COA ensures that a cluster of cells interact with one another more or less regularly over an extended period of time. This is because COA keeps the cells

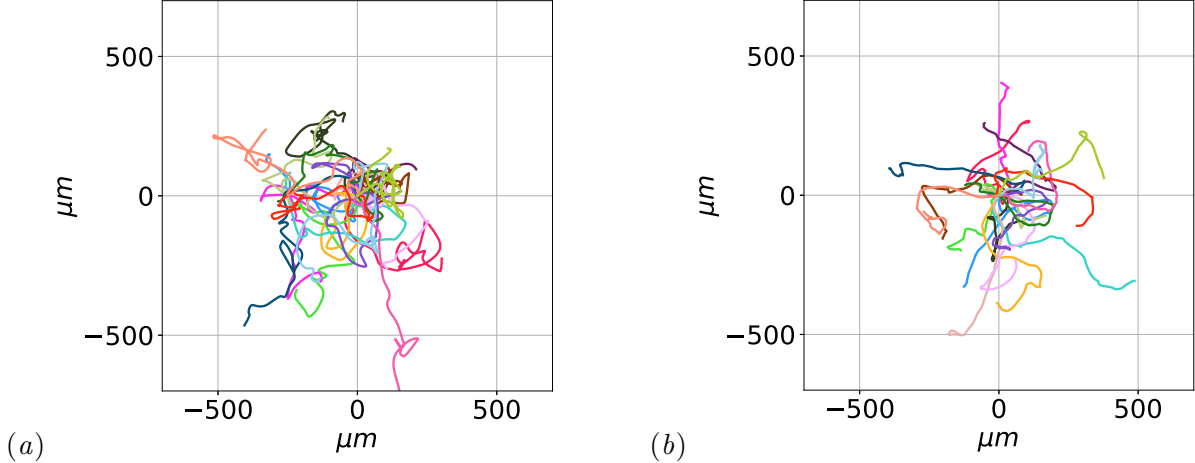


Figure 2: (a) Trajectories of 20 repeated simulations of a single cell over 10 hours in the absence of chemoattractant ( $M = 0$ ). The trajectories show an averaged persistence ratio  $R_p = 0.24$  and averaged persistence time  $T_p = 23$  min. (b) Similar trajectories of the centroid of a 16-cell cluster, with  $R_p = 0.45$  and  $T_p = 81$  min.

in a coherent cluster so they do not scatter, while CIL separates two neighboring cells immediately after contact such that they will be able to make another contact shortly. A consequence of these repeated contacts is that each member cell develops persistence of polarity (POP), and the cluster exhibits a stronger directional persistence in its collective movement.

To illustrate this emergent POP, Fig. 2 compares the trajectories of 20 runs of a single cell with those of a 16-cell cluster. A representative run of the cluster is illustrated in Movie S2. In the absence of a chemoattractant ( $M = 0$ ), of course, neither the single cell nor the cluster shows directional movement over a long time; both essentially execute random walks. Nevertheless, the cluster shows increased persistence as the centroid trajectories in Fig. 2(b) exhibit relatively long straight segments, while that of single cells in Fig. 2(a) features tighter turns and more frequent changes in direction. To quantify the elevated POP, we define a persistence ratio  $R_p$  as that between the end-to-end distance and the contour length of the centroid trajectory over the entire duration of the simulation (10 hours for all results reported), and a persistence time  $T_p$  as the autocorrelation time in directional displacement of the group centroid [9]. Figure 3 shows that in general,  $T_p$  and  $R_p$  increase with cluster size  $N_c$ , and we claim that POP does so as well. This trend can also be observed in the increase of protrusion lifetime in clusters of increasing size, especially in comparison with solitary cells (Fig. S3 in SI).

The cluster exhibits increased directional persistence in the motion of its centroid because of

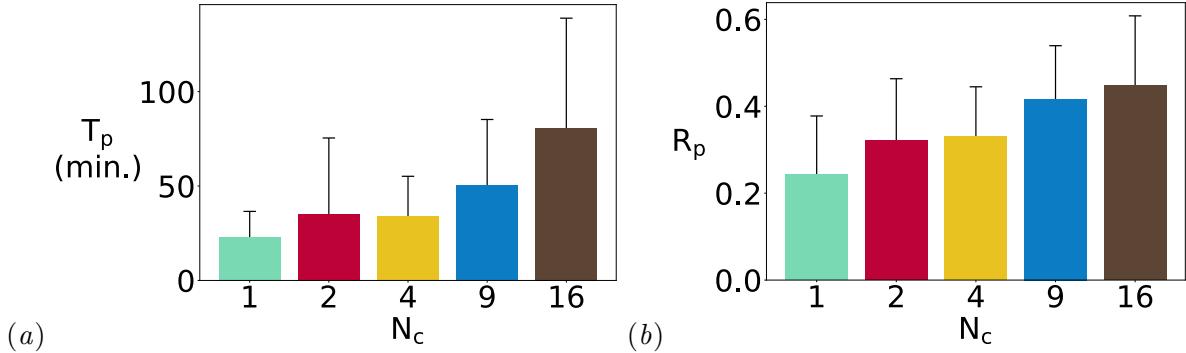


Figure 3: Even in the absence of a chemoattractant ( $M = 0$ ), cell clusters show increased directional persistence in their centroid motion, and the effect increases with cluster size  $N_c$ . (a) The persistence time  $T_p$  increases by roughly 4 times from  $N_c = 1$  to  $N_c = 16$ . (b) The persistence ratio  $R_p$  nearly doubles from  $N_c = 1$  to  $N_c = 16$ . In this figure, the error bars indicate the standard deviation among the 20 runs.

POP of its member cells, which emerges from the simultaneous action of CIL and COA. CIL suppresses Rac1 activity in cells, especially the appearance of new Rac1 “hotspots” on the cell membrane that may potentially grow and outcompete existing protrusion fronts. With CIL, therefore, random bursts in Rac1 activation are less effective in perturbing a cell’s current polarization. COA primarily serves to renew CIL interactions, by maintaining cell-cell proximity and a relatively stable cell density.

That CIL and COA cooperate to suppress random Rac1 bursts to promote POP as an emergent property is consistent with earlier experiments on single-cell persistence. For example, Pankov *et al.* [17] suppressed Rac1 activity globally by using drugs, and observed increased persistence in directional migration of single fibroblast cells. Bass *et al.* [18] and Matthews *et al.* [19] demonstrated that Syndecan-fibronectin binding, which suppresses Rac1 activity, increases persistence in migration of isolated fibroblasts and NCCs. In our situation, inhibition of Rac1 hotspots is achieved not by drug treatment or via the Syndecan pathway, but by the simultaneous action of CIL and COA.

Although a cluster exhibits longer persistence times than a single cell, the cluster centroid still exhibits a random walk over long times (Fig. 2b) in the absence of a chemoattractant. The presence of even a shallow chemoattractant gradient may bias the collective migration and lead to directional chemotaxis, as will be shown in subsection 3.4.

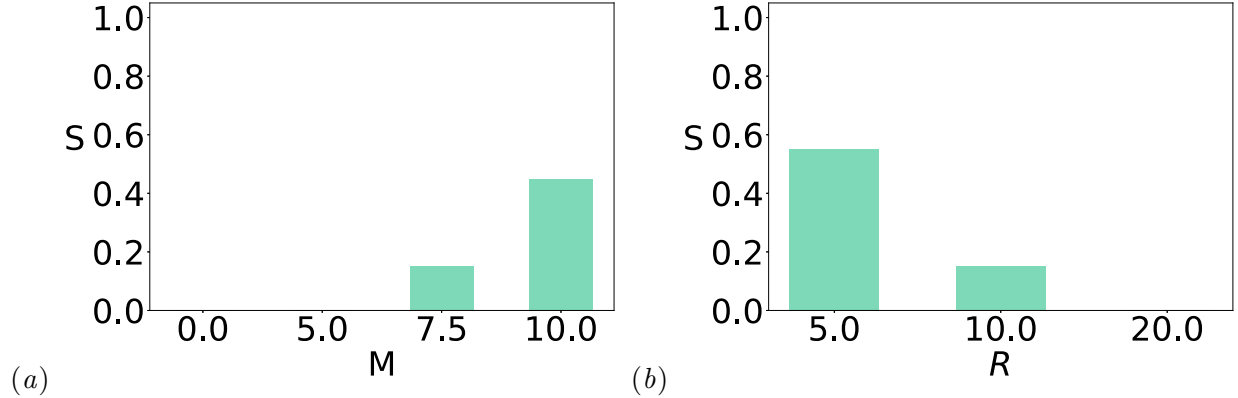


Figure 4: (a) For the standard set of parameters, a single cell’s chemotaxis success rate  $S$  increases with the gradient of the chemoattractant  $M$ . (b) At  $M = 7.5$ , increasing the magnitude of random noise  $R$  reduces chemotactic success.

### 3.3 Solitary cell motility in the presence of a chemoattractant

As a baseline for probing the group advantage in collective chemotaxis, we first study the behavior of a single cell in a chemoattractant gradient. Figure 2(a) shows the run-and-tumble motion of a cell in the absence of an external gradient ( $M = 0$ ). As we gradually increase this gradient, the cell should eventually become responsive to it. This is indeed the case as Fig. 4(a) demonstrates. As we increase the parameter  $M$  while keeping all the other parameters fixed at their standard values, we see the gradual emergence of chemotaxis, with a success rate  $S \approx 0.45$  at  $M = 10$ . Movie S3 shows a representative simulation of a single cell chemotaxing at  $M = 10$ .

The result suggests that the external chemotactic guidance competes with the internal random bursts in Rac1 activity for cell repolarization. To test this further, we hold the strength of chemoattractant gradient at  $M = 7.5$ , and vary the magnitude of the internal noise  $R$  of Rac1 activation (cf. discussion of Eq. S8 in the SI). Indeed, increasing  $R$  decreases single cell chemotactic success (Fig. 4b). A similar series of tests shows that increasing the frequency of the random perturbation while keeping its magnitude fixed also tends to suppress the success of chemotaxis. This trend holds up to a certain frequency. At even higher frequencies, however, the cell can no longer respond fast enough and stops repolarizing according to the noise.

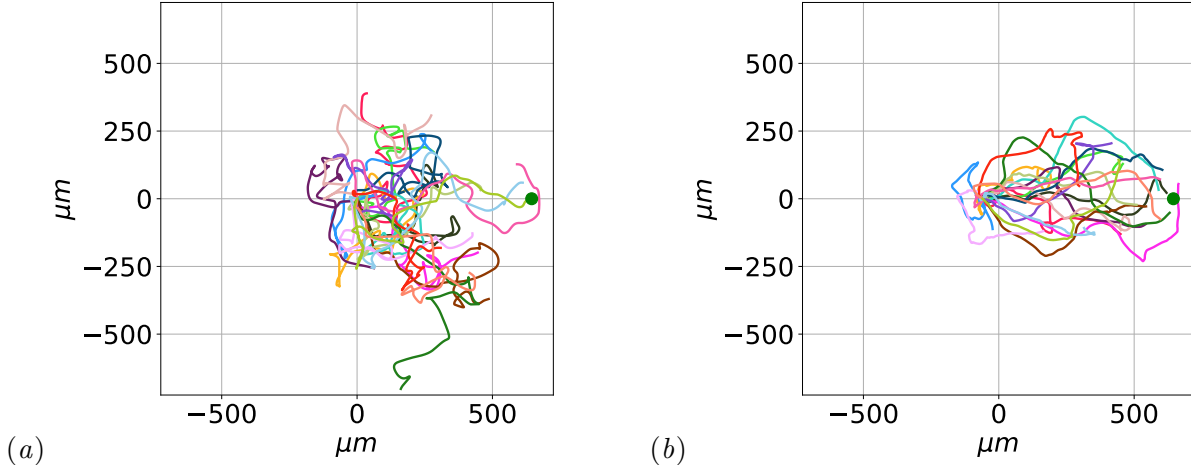


Figure 5: (a) The trajectories of 20 simulations of a single cell in a weak chemoattractant gradient at  $M = 7.5$ . The persistence ratio  $R_p = 0.31$ , and the persistence time  $T_p = 29$  min. (b) Trajectories for the centroid of a cluster of 16 cells in the same external gradient.  $R_p = 0.65$ ,  $T_p = 243$  min.

### 3.4 Collective chemotaxis of a cluster

To investigate the group advantage in collective chemotaxis, let us first focus on a weak gradient  $M = 7.5$  at which a single cell exhibits a low success rate  $S \approx 0.15$  (see Fig. 4a). Figure 5 compares the trajectories of a single cell and of a 16-cell cluster for 20 simulations. While the single cell moves along highly tortuous paths, the cluster exhibits more directional paths toward the source of the chemoattractant. The persistence ratio  $R_p$  is 0.31 for a single cell. The cell cluster possesses an elevated  $R_p = 0.65$ , more than double that of a single cell. Besides, the persistence time  $T_p$  increases by more than 8 times. Thus, the model has demonstrated a clear group advantage.

To illustrate the collective behavior of the cells in a cluster, Fig. 6 shows three snapshots of the 16-cell cluster for one of the trajectories of Fig. 5(b). Because of the frequent contact among the cells in the interior of the cluster, they tend to carry high RhoA and low Rac1 on the membrane, thus not showing clear polarization. Meanwhile, the cells at the periphery of the cluster tend to protrude outward. These observations are consistent with the *in vitro* experiment of Theveneau *et al.* [3]. Movie S4 in the SI gives a more detailed and informative depiction of the cluster's collective chemotaxis. The successful chemotaxis of the 16-cell cluster can be contrasted with the failure of a single cell in the same gradient, shown in Movie S5.

The group advantage has its root in the directionally biased Rac1 protrusion in favor of the external gradient. Following Theveneau *et al.* [3], we illustrate this directional bias by the angular

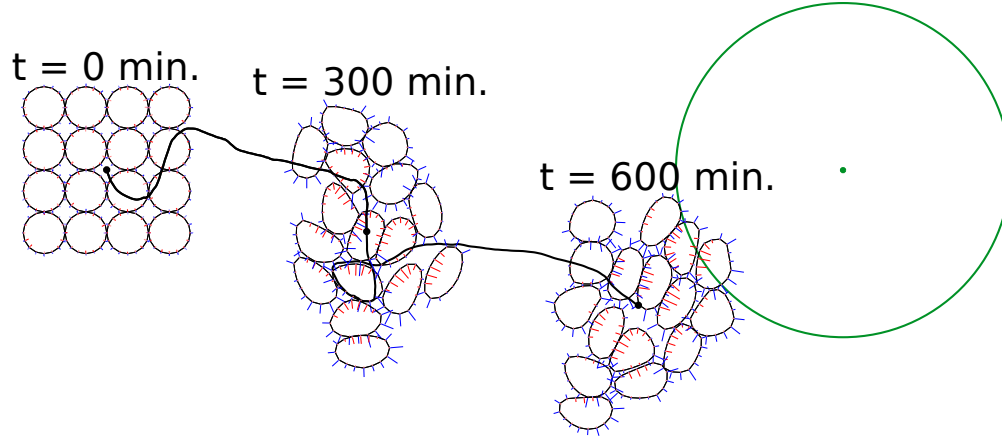


Figure 6: Snapshots of the 16-cell cluster at three instants of its collective chemotaxis at  $M = 7.5$ . On the outline of each cell, the outward and inward line segments indicate the local Rac1 and RhoA levels as in Fig. 1, and the solid curve marks the trajectory of the cluster’s centroid. The green circle to the right marks the “target zone” centered at the source of the chemoattractant.

distribution of the averaged number of Rac1 protrusions for a single cell and for each cell in a 16-cell cluster (Fig. 7). For the current purpose, a vertex is identified as protrusive if its active Rac1 exceeds 25% of the maximum among all vertices and this percentage exceeds that for active RhoA on that vertex. A protrusion is then defined as a contiguous sequence of protrusive vertices, with an orientation equal to that of the central vertex in the protrusion if the number of vertices in the protrusion is odd, or the average of the orientation of the two central vertices in the protrusion if the number of vertices is even. The total number of protrusions in a certain bracket of orientation angle is then tallied over the length of the simulation and averaged among the cells and the 20 realizations of each simulation. While the distribution for a single cell is not isotropic, it does not show a strong bias toward the gradient direction ( $0^\circ$  in Fig. 7a). In fact, there appears to be a modest bias toward  $\theta = 22.5^\circ$ . Therefore, the single cell is relatively insensitive to the external gradient at a strength of  $M = 7.5$ . In contrast, the 16-cell clusters exhibit an unequivocal preference for extending protrusions toward the source of the chemoattractant, and the protrusive vertices are longer-lived (Fig. S4 in SI). These plots confirm our conclusion of subsection 3.2: CIL and COA cooperate to ensure continual intercellular contacts that dampen the random activity of Rac1 and enhance persistence of polarity for each cell. In turn, POP sensitizes the group to an external chemoattractant in favor of collective chemotaxis. Now that we have demonstrated the existence of group advantage in chemotaxis, we will explore its various aspects in the following.

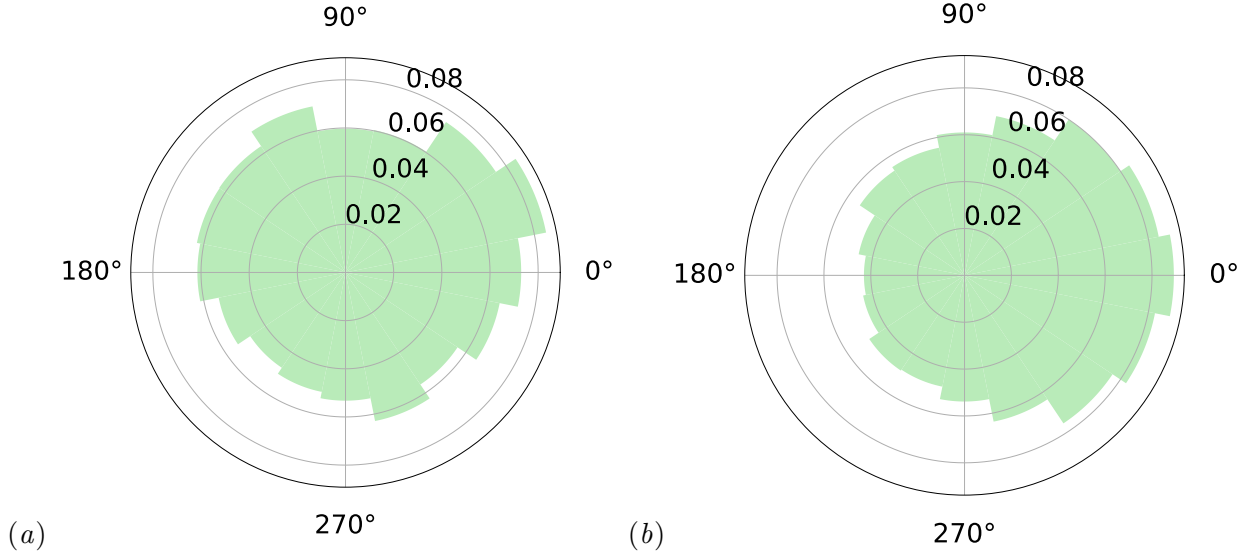


Figure 7: Comparison of the angular distribution of the protrusions (a) on a single cell in a chemoattractant gradient  $M = 7.5$ ; (b) averaged for each cell within a cluster of 16 cells in the same gradient. The orientational angle  $\theta = 0^\circ$  points toward the source of the chemoattractant. The protrusion numbers are averaged among 20 realizations in each case, over the chemotactic process of 10 hours. They have been scaled into a probability for each  $22.5^\circ$  sector, indicated atop the concentric circles, such that the total probability over all sectors normalizes to 1.

**A. Group size effect.** The group advantage generally increases with group size  $N_c$ . Figure 8 illustrates this point through the group persistence ratio  $R_p$  and the success rate of chemotaxis  $S$ . Note that even without chemoattractant ( $M = 0$ ), a cluster exhibits greater persistence as discussed in Subsection 3.2 (cf. Fig. 3). As  $M$  increases to 5 and 7.5, the group advantage becomes more distinct both in  $R_p$  and  $S$ . Not surprisingly, as the external gradient becomes strong ( $M = 10$ ), even the single cell starts to react consistently to it. Then the contrast between  $N_c = 16$  and  $N_c = 1$  becomes less distinct, even though larger clusters still tend to enjoy a stronger chemotactic efficiency. We have simulated chemotaxis of larger groups up to  $N_c = 49$ . The group advantage increases with group size in general, but appears to saturate for the largest groups, with  $R_p$  and  $S$  both approaching 0.9 (Fig. S5). This resembles the saturation of the efficiency of spontaneous collective migration in the absence of chemoattractants [9].

We can interpret the group size effect in terms of the frequency of cell-cell interactions. The dampening of random Rac1 activity depends upon the frequency of CIL interactions in particular. We ask if a larger group exhibits a pronounced group advantage owing to a higher frequency of such interactions. Indeed, the interaction frequency increases with the group size  $N_c$ , as seen in

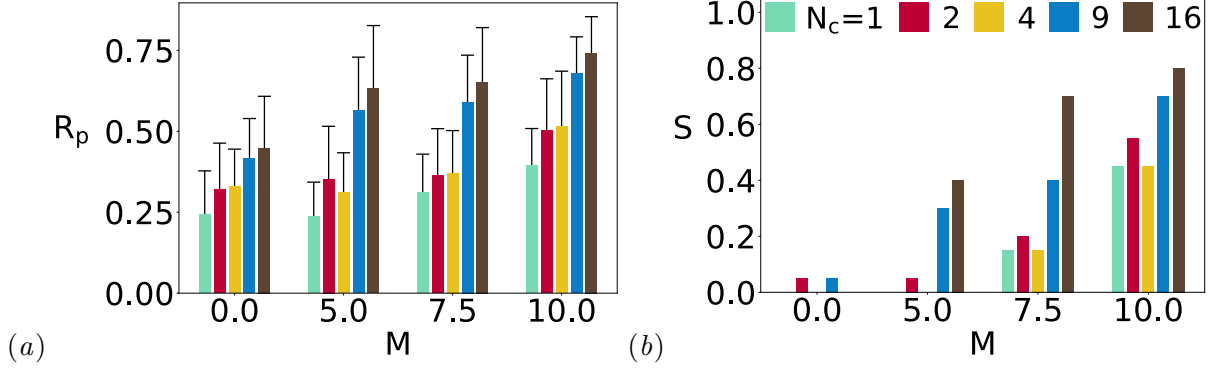


Figure 8: Group advantage in collective chemotaxis increases with group size. (a) The group centroid persistence ratio  $R_p$  for various group sizes at increasing  $M$  values. The error bars indicate the standard deviation among the 20 runs. (b) The group success rate  $S$  under the same conditions. The same legend for  $N_c$  applies to (a) as well.

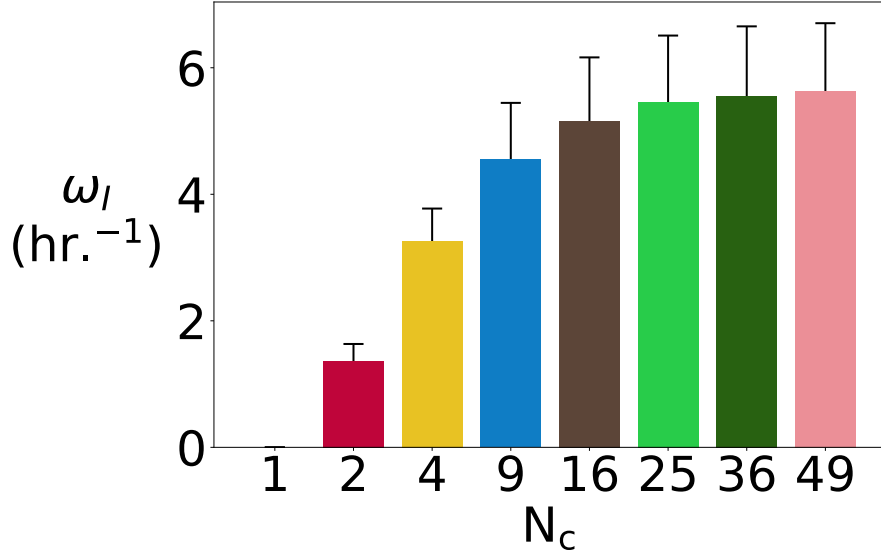


Figure 9: Averaged frequency of CIL interaction per cell as a function of group size. The frequency  $\omega_I$  increases with  $N_c$  for smaller groups, but saturates for larger groups. In this figure, the error bars indicate the standard deviation computed from all instances of pairwise interaction during the 20 runs for each  $N_c$ .

Fig. 9, but saturates for larger groups. Geometrically, the interaction frequency is limited by how many neighbors can fit around a given cell, and hence the saturation for larger groups.

**B. Chemotactic speed and directionality.** To study how the speed of chemotaxis varies with group size, we first distinguish the centroid speed  $v$  of a cluster from its “directional component”  $v_x$ . The average speed  $v$  is computed from the displacement of the cluster centroid over the 10-hour simulation time, and  $v_x$  is its horizontal component. Since the cluster is initially placed directly to the left of the source of chemoattractant, the  $x$  component of the displacement is up the

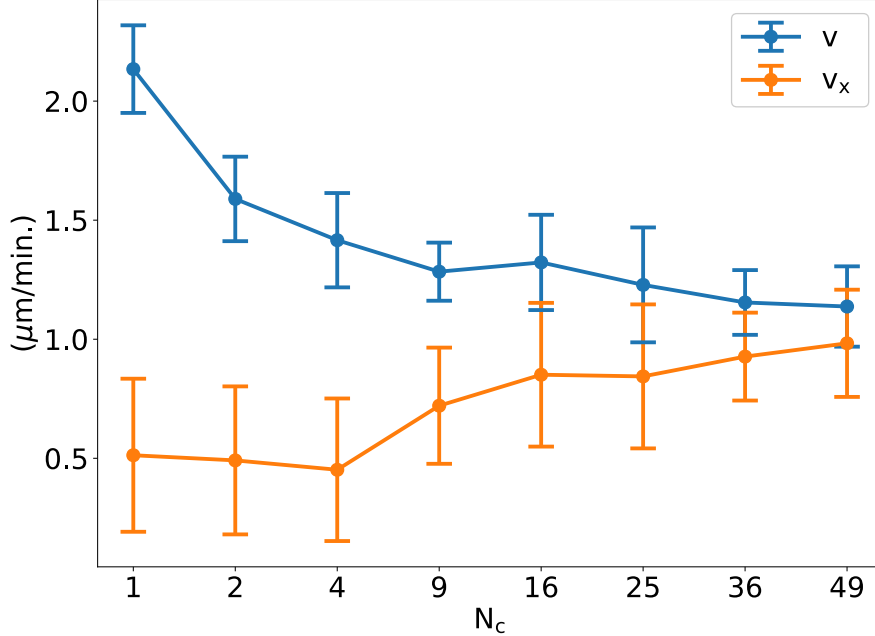


Figure 10: Variation of group speed and velocity of movement towards chemoattractant with respect to group size  $N_c$ . While the instantaneous speed of the cluster centroid  $v$  declines with  $N_c$ , its “directional component”  $v_x$ , toward the source of chemoattractant, increases with  $N_c$ . For each  $N_c$ , the data point and error bars represent the average and standard deviation of the group speed sampled over each time step ( $\Delta t = 2$  s) over all simulations.

chemoattract gradient toward the source. Figure 10 depicts both quantities, time-averaged over the duration of the chemotaxis, for a single cell and clusters of various sizes. For a single cell,  $v$  is much greater than  $v_x$ . The single cell moves relatively fast, but in a tortuous path that advances little toward the source of chemoattractant. With increasing  $N_c$ , the two curves converge toward each other, signifying increased directionality in chemotaxis. Although the larger clusters move more slowly in terms of the absolute speed  $v$ , their motion is better oriented toward the chemoattractant source. For the largest cluster tested ( $N_c = 49$ ), the speed of directional chemotaxis is roughly  $v_x = 0.98 \mu\text{m}/\text{min}$ , less than half of the single-cell speed of  $v = 2.13 \mu\text{m}/\text{min}$ . Also  $v_x$  exhibits a saturation with  $N_c$ , similar to other indices of the group advantage (Fig. 8, Fig. S5). If the chemoattractant is removed ( $M = 0$ ), the average  $v_x$  reduces nearly to zero as expected, while the group speed  $v$  decreases only moderately for the larger clusters and even less for the smaller ones (Fig. S6).

We have found only a few reports of chemotactic speed for cranial NCCs. From Fig. 3C and Movie S5 of Theveneau *et al.* [3], we can estimate a value of  $v_x \sim 1.5 \mu\text{m}/\text{min}$ , about 50%

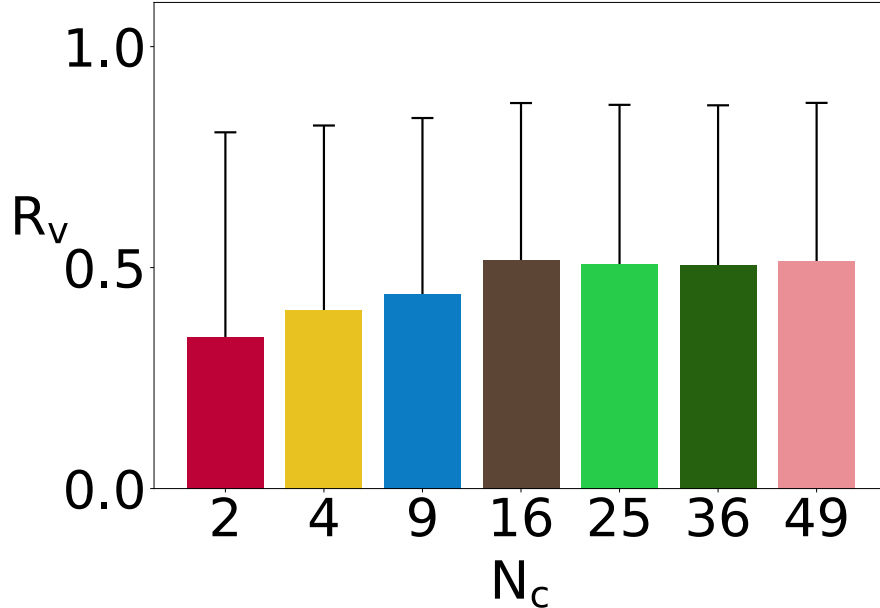


Figure 11: Chemotaxing clusters exhibit velocity alignment as the cross-correlation  $R_v$  of the velocity vector of pairs of neighbors increases with the cluster size  $N_c$  for smaller clusters and saturates for larger ones. The cell velocity vector is calculated from its centroid displacement over 5 min intervals, and  $R_v$  is computed using 4 nearest neighboring cells. The error bars show the standard deviation among all  $R_v$  data collected from all the 20 runs for each  $N_c$ .

larger than our model prediction. This discrepancy can be due to various reasons, including the assumptions and simplifications in the model. In addition, it is not possible to match the spatial distribution of the chemoattractant between the experiment and the modeling. Our model assumes a constant gradient while the experiment has a Sdf1-soaked bead in a planar space, presumably producing a radially decaying gradient. The magnitude of the gradient in the experiment has not been quantified or reported. Despite the uncertainties, the model predicts a chemotactic velocity  $v_x$  on the same order of magnitude as observed experimentally. Note that the comparison of the chemotactic speed is not a parameter fitting exercise. At the outset we have tuned the mechanical parameters to reproduce a single-cell speed of  $3 \mu\text{m}/\text{min}$  during the “run-phase” of its trajectory, according to experimental measurements [15, 16]. Afterwards, the standard set of parameters are not adjusted further.

Analyzing the instantaneous velocity of the cells during collective chemotaxis, we have noticed what appears to be alignment of velocity among the neighbors. Figure 11 plots the cross-correlation  $R_v$  of cell velocity vectors in cell clusters of increasing size (for details of computing  $R_v$  see SI, Sec. 4). The cell motion becomes more aligned among neighbors in larger clusters that possess

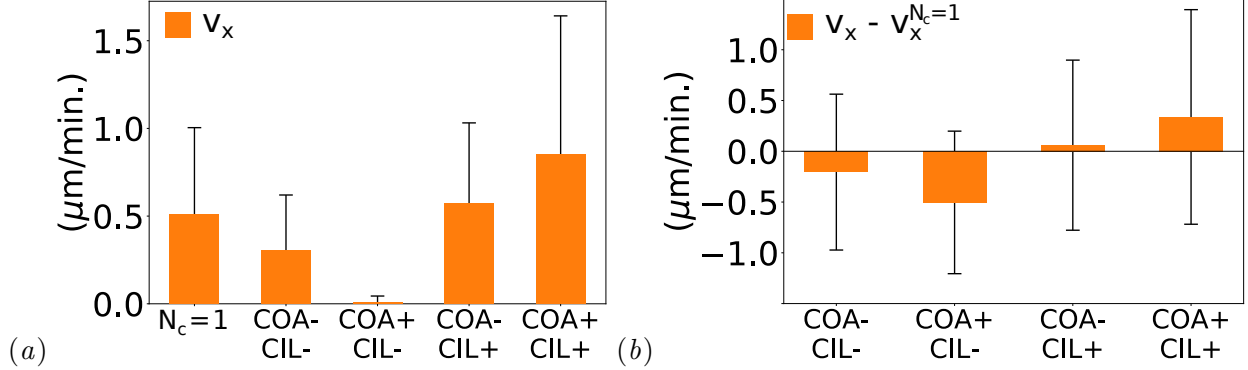


Figure 12: Effect of CIL and COA knockdowns on the directional migration of a 16-cell cluster. (a) Directional speed  $v_x$  for the three CIL and/or COA knockdown cases compared with those of a single cell ( $N_c = 1$ ) and of the control case that has CIL and COA intact. (b) Group advantage, represented by the difference of  $v_x$  from that of the single cell, for the knockdowns and the control case. It is severely impaired by deficiency in CIL or COA. The column and error bar represent the mean and standard deviation of each data set collected as in Fig. 10, consisting of the cluster centroid velocity at each time step of each simulation. A bootstrap analysis over the large samples of velocity values (18,000 for  $N_c = 1$  and 360,000 for the 16-cell clusters) yields a 99% confidence interval for the mean velocity of  $\pm 5.0 \times 10^{-3} \mu\text{m}/\text{min}$  for  $N_c = 1$ , and  $\pm 1.3 \sim 3.4 \times 10^{-3} \mu\text{m}/\text{min}$  for the  $N_c = 16$  clusters in both plots.

more persistent directional chemotaxis, although the degree of alignment seems to saturate for  $N_c \geq 16$ . This recalls the velocity alignment in models for swarms of interacting particle [20, 21], which produces directional collective motion. But the similarity is superficial. In the swarming models, alignment rules are postulated as the starting point of the modeling. They are the direct cause of collective motion for the swarm. Our model posits no explicit alignment rules; velocity alignment appears here as an emergent property of a NCC cluster in which cell-cell interaction leads to resistance to noisy perturbations in the Rac1-RhoA signaling pathway.

### C. Loss of group advantage.

As the group advantage emerges from the increased POP of individuals in a cluster, we ask if the advantage might be negated through the reduction of POP. This is investigated by three knockdown studies in which we suppress CIL only (COA+/CIL-), COA only (COA-/CIL+) or both (COA-/CIL-) in the chemical kinetics of the model. Movies S6 and S7 show two representative simulations of the behavior of a 16-cell cluster for the COA+/CIL- and COA-/CIL+ cases, respectively. As expected, POP is compromised in all three cases and the group advantage weakens or even disappears. In the CIL knockdown (COA+/CIL-), the cells clump into a dense cluster that fails to chemotax, much as observed in the experiment of Theveneau *et al.* [3] (Fig. 5 and

Movie S8 therein). The centroid directional speed  $v_x \approx 0$  in this case (Fig. 12a). Similarly, the COA knockdowns (COA-/CIL- and COA-/CIL+) show cells scattering in space as in the experimental images of Carmona-Fontaine *et al.* [6] (Fig. 5 and Movie S6 therein). Thus the cluster loses its coherence and group advantage, with a relatively low  $v_x$  comparable to that of a single cell (Fig. 12ab). Relative to the chemotaxis of a single cell, only the control case (COA+/CIL+) enjoys an appreciably greater  $v_x$  (Fig. 12b). Incidentally, as the cluster scatters with COA-, individual cells may wander into the target zone by chance. This event would register as a “success” in our scheme of calculating the success rate  $S$ . This illustrates a limitation in our definition of  $S$ ; it is a useful index only for a cohesive cluster.

As we have demonstrated in Subsection 3.3, the chemotaxis of a single cell can be viewed as the external influence of the chemoattractant gradient overwhelming the intrinsic noise of the cell’s repolarization, and can be abolished by increasing either the magnitude or the frequency of random bursts in Rac1 activity. A similar scenario occurs for a cluster; its chemotaxis is weakened and eventually abolished as the frequency or magnitude of random Rac1 activity increases (see Fig. S7 and Movie S8 in the SI). This reaffirms our view of chemotaxis, in the context of the current model at least, as the competition between the external gradient and the internal noise that promotes repolarization.

## 4 Discussion

A key point that we have learned through this modeling exercise is that the chemotaxis of a single cell can be viewed as a competition between the directional influence of the external gradient and the randomizing influence of an internal noise. The latter is represented in our model by perturbations to the Rac1 activation rate on randomly selected membrane nodes at random intervals sampled from a normal distribution. Thus, less frequent or weaker random perturbation leads to less frequent repolarization of Rac1 fronts and enhanced single-cell chemotaxis, and vice versa. This observation is consistent with prior experiments that suppressed Rac1 activity by Rac1 inhibitors [17] and by Syndecan-fibronectin binding [18, 19].

A second conclusion of this study is that group advantage in chemotaxis emerges from cell-cell interactions. More specifically, the simultaneous action of contact inhibition of locomotion

(CIL) and co-attraction (COA) ensures continual interaction between neighboring cells, which suppresses new Rac1 hotspots that could otherwise grow and outcompete existing protrusions to produce a repolarization. Thus, CIL and COA produce a persistence of polarity (POP) against random repolarization, which allows a cluster of NCCs to chemotax up a shallow gradient of chemoattractant to which a single cell would be insensitive. This is how our model explains the curious group advantage in chemotaxis observed *in vitro*. It is therefore an “emergent property” of the group.

In a previous study [9], we used the CIL+COA→POP mechanism to explain another emergent behavior in clusters of neural crest cells: their spontaneous persistent migration down a confining channel in the absence of any external chemoattractant [6]. These two scenarios form an intriguing parallel to each other. In the spontaneous collective migration case, POP sensitizes an NCC cluster to an initial geometric bias due to confinement at the channel’s end, to which an isolated cell would be unresponsive. In collective chemotaxis, on the other hand, POP sensitizes the cluster to a weak gradient to which an isolated cell would be unresponsive.

It is instructive to compare our GTPase-based model with existing models. Recalling Camley’s categorization of previous phenomenological models [2], one may notice connections of our model to two of the categories. Insofar as our model exhibits apparent velocity alignment among neighbors, it resembles the “collective susceptibility” models. But no such alignment rule is postulated as in the phenomenological models. Rather, the apparent alignment emerges as an outcome of the biochemical kinetics postulated on the intracellular level. Note, however, the newer experimental evidence for leader-follower roles in NCC chemotaxis under certain conditions [22, 23], especially for trunk neural crests [24, 25]. Thus, explicit neighbor alignment may be an important strategy for the chemotaxis of certain NCCs under different conditions.

In the sense that each member of a cluster may move in a different direction at any moment, while the centroid of the cluster follows a more persistent motion up the chemoattractant gradient, our model also resembles the “many wrongs” model discussed by Camley [2]. However, in our model, group advantage does not arise from averaging the measurement of gradients by the members, as is central to the “many wrongs” concept, but from elevated resistance to an internal noise promoting random repolarization. Therefore, noise is introduced at different points of the chemotaxis pathway in the two models. In the many-wrongs model, the noise may arise from sensing of the external

gradient, e.g. from the stochasticity of ligand-receptor binding [2]. In our model, on the other hand, the noise comes from random perturbations to the intracellular Rac1 kinetics, which, if sufficiently strong or frequent, can defeat the directional cue of the chemoattractant. In reality, both kinds of noise probably coexist, and both types of modeling may complement each other.

The above discussion of the source of noise—random noise in intracellular Rac1 bursts or in sensing the external gradient—suggests new experiments to test the hypothesis of our model against that of previous modeling based, e.g., on the “many wrongs” idea. Pankov *et al.* [17] was able to improve persistence of single fibroblast cells by applying drug to reduce random Rac1 activity. Following the same approach, we ask if cranial neural crest cell’s response to a chemoattractant can be improved by application of similar drugs. If the answer turns out to be affirmative, then the main obstacle to chemotaxis in a shallow gradient is random Rac1 activity inside the cell, and the experiment will have validated our model hypothesis. A negative answer, on the other hand, will have cast doubt on our model’s hypothesis for the group advantage. There will likely be other factors at play, e.g., noise in gradient sensing, that we have failed to take into account.

Finally, we comment on the merits of what is called “mechanistic modeling” here, in relation to the agent-based or rule-based paradigm. Agent-based models can be used to great advantage in testing hypothesized rules of interaction when little is known of the underlying biochemical mechanisms [22,26]. But when a certain amount is known about the biochemistry, it is possible to build a mechanistic model that is based more directly on such biological underpinnings. A benefit of this direct connection is to suggest new experiments to test the mechanisms, as illustrated in the preceding paragraph. In the mean time, such mechanistic modeling will likely be more specific to cell types and biological processes, whereas a rule-based model can be more general and inclusive. Biological reality is often characterized by its rich and diverse mechanisms. For example, while trunk NCCs seem to chemotax using a leader-follower strategy, cranial NCCs appear to be homogeneous and rely on cell-cell interactions to realize collective migration [24,25]. More recent work on cranial NCCs suggests a distinct mechanism based on a supracellular actomyosin ring that contracts the rear of the cluster [27]. Thus, a more mechanistic approach as advocated here may be useful in accounting for such diversity and specificity.

**Author Contributions:** BHM and JJF designed the research. BHM wrote the code and carried

out the simulations, and BHM and JJF analyzed the data and wrote the paper.

**Acknowledgement:** The authors acknowledge financial support by the Natural Sciences and Engineering Research Council of Canada (Grant no. 2019-04162). We wish to thank Leah Edelstein-Keshet for her suggestions on various aspects of the project, and for critiquing an earlier version of the manuscript. We also thank Brian Camley, Arnold Hayer, Paul Kulesa, Philip Maini and Roberto Mayor for stimulating discussions.

## References

- [1] R. Winklbauer, A. Selchow, M. Nagel, B. Angres, Cell interaction and its role in mesoderm cell migration during xenopus gastrulation, *Dev. Dyn.* 195 (1992) 290–302.
- [2] B. A. Camley, Collective gradient sensing and chemotaxis: modeling and recent developments, *J. Phys.: Condens. Matter* 30 (2018) 223001.
- [3] E. Theveneau, L. Marchant, S. Kuriyama, M. Gull, B. Moepps, M. Parsons, R. Mayor, Collective chemotaxis requires contact-dependent cell polarity, *Dev. Cell* 19 (2010) 39–53.
- [4] G. Malet-Engra, W. Yu, A. Oldani, J. Rey-Barroso, N. Gov, G. Scita, L. Dupré, Collective cell motility promotes chemotactic prowess and resistance to chemorepulsion, *Curr. Biol.* 25 (2015) 242 – 250.
- [5] D. Ellison, A. Mugler, M. D. Brennan, S. H. Lee, R. J. Huebner, E. R. Shamir, L. A. Woo, J. Kim, P. Amar, I. Nemenman, A. J. Ewald, A. Levchenko, Cell–cell communication enhances the capacity of cell ensembles to sense shallow gradients during morphogenesis, *Proc. Natl. Acad. Sci. U.S.A.* 113 (2016) E679–E688.
- [6] C. Carmona-Fontaine, E. Theveneau, A. Tzekou, M. Tada, M. Woods, K. M. Page, M. Parsons, J. D. Lambris, R. Mayor, Complement fragment c3a controls mutual cell attraction during collective cell migration, *Dev. Cell* 21 (2011) 1026–1037.
- [7] A. J. Ridley, Rho GTPase signalling in cell migration, *Curr. Opin. Cell Biol.* 36 (2015) 103–112.

- [8] W.-J. Rappel, L. Edelstein-Keshet, Mechanisms of cell polarization, *Curr. Opin. Syst. Biol.* 3 (2017) 43–53.
- [9] B. Merchant, L. Edelstein-Keshet, J. J. Feng, A Rho-GTPase based model explains spontaneous collective migration of neural crest cell clusters, *Dev. Biol.* 444 (2018) S262–S273.
- [10] Y. Mori, A. Jilkine, L. Edelstein-Keshet, Wave-pinning and cell polarity from a bistable reaction-diffusion system, *Biophys. J.* 94 (2008) 3684–3697.
- [11] B. Vanderlei, J. J. Feng, L. Edelstein-Keshet, A computational model of cell polarization and motility coupling mechanics and biochemistry, *Multiscale Model. Simul.* 9 (2011) 1420–1443.
- [12] B. Huang, M. Lu, M. K. Jolly, I. Tsarfaty, J. Onuchic, E. Ben-Jacob, The three-way switch operation of Rac1/RhoA GTPase-based circuit controlling amoeboid-hybrid-mesenchymal transition, *Sci. Rep.* 4 (2014) 6449.
- [13] S. Lim, H. Nam, J. S. Jeon, Chemotaxis model for breast cancer cells based on signal/noise ratio, *Biophys. J.* 115 (2018) 2034 – 2043.
- [14] W. R. Holmes, L. Edelstein-Keshet, Analysis of a minimal Rho-GTPase circuit regulating cell shape, *Phys. Biol.* 13 (2016) 046001.
- [15] C. Carmona-Fontaine, H. K. Matthews, S. Kuriyama, M. Moreno, G. A. Dunn, M. Parsons, C. D. Stern, R. Mayor, Contact inhibition of locomotion in vivo controls neural crest directional migration, *Nature* 456 (2008) 957–961.
- [16] M. L. Woods, C. Carmona-Fontaine, C. P. Barnes, I. D. Couzin, R. Mayor, K. M. Page, Directional collective cell migration emerges as a property of cell interactions, *PloS One* 9 (2014) e104969.
- [17] R. Pankov, Y. Endo, S. Even-Ram, M. Araki, K. Clark, E. Cukierman, K. Matsumoto, K. M. Yamada, A Rac switch regulates random versus directionally persistent cell migration, *J. Cell Biol.* 170 (2005) 793–802.
- [18] M. D. Bass, K. A. Roach, M. R. Morgan, Z. Mostafavi-Pour, T. Schoen, T. Muramatsu, U. Mayer, C. Ballestrem, J. P. Spatz, M. J. Humphries, Syndecan-4–dependent Rac1 regulation

- determines directional migration in response to the extracellular matrix, *J. Cell Biol.* 177 (2007) 527–538.
- [19] H. K. Matthews, L. Marchant, C. Carmona-Fontaine, S. Kuriyama, J. Larraín, M. R. Holt, M. Parsons, R. Mayor, Directional migration of neural crest cells in vivo is regulated by Syndecan-4/Rac1 and non-canonical Wnt signaling/RhoA, *Development* 135 (2008) 1771–1780.
- [20] T. Vicsek, A. Czirók, E. Ben-Jacob, I. Cohen, O. Shochet, Novel type of phase transition in a system of self-driven particles, *Phys. Rev. Lett.* 75 (1995) 1226–1229.
- [21] M. C. Marchetti, J. F. Joanny, S. Ramaswamy, T. B. Liverpool, J. Prost, M. Rao, R. A. Simha, Hydrodynamics of soft active matter, *Rev. Mod. Phys.* 85 (2013) 1143–1189.
- [22] R. McLennan, L. Dyson, K. W. Prather, J. A. Morrison, R. E. Baker, P. K. Maini, P. M. Kulesa, Multiscale mechanisms of cell migration during development: theory and experiment, *Development* 139 (2012) 2935–2944.
- [23] R. McLennan, L. J. Schumacher, J. A. Morrison, J. M. Teddy, D. A. Ridenour, A. C. Box, C. L. Semerad, H. Li, W. McDowell, D. Kay, P. K. Maini, R. E. Baker, P. M. Kulesa, VEGF signals induce trailblazer cell identity that drives neural crest migration, *Dev. Biol.* 407 (2015) 12–25.
- [24] J. Richardson, A. Gauert, L. B. Montecinos, L. Fanlo, Z. M. Alhashem, R. Assar, E. Marti, A. Kabla, S. Härtel, C. Linker, Leader cells define directionality of trunk, but not cranial, neural crest cell migration, *Cell Rep.* 15 (2016) 2076 – 2088.
- [25] E. Theveneau, C. Linker, Leaders in collective migration: are front cells really endowed with a particular set of skills?, *F1000Res.* 6 (2017) 1899.
- [26] C. M. Glen, M. L. Kemp, E. O. Voit, Agent-based modeling of morphogenetic systems: Advantages and challenges, *PLoS Comput. Biol.* 15 (2019) e1006577.
- [27] A. Shellard, A. Szabó, X. Trepast, R. Mayor, Supracellular contraction at the rear of neural crest cell groups drives collective chemotaxis, *Science* 362 (2018) 339–343.

# Supporting Information for “A Rho-GTPase based model explains group advantage in chemotaxis through suppression of random repolarization”

Brian Merchant<sup>1</sup> and James J. Feng<sup>1,2\*</sup>

<sup>1</sup> Department of Mathematics, University of British Columbia, Vancouver, BC V6T 1Z2, Canada

<sup>2</sup> Department of Chemical and Biological Engineering, University of British Columbia, Vancouver, BC V6T 1Z3, Canada

## 1 Kinetic model

The polarization of the cell is controlled by the autocatalysis of Rac1 and RhoA, as well as their mutual inhibition [1, 2]. Our model tracks fractions of Rac1 and RhoA in their membrane-bound active and inactive states, as well as in the cytosol. The total amount of Rac1 is  $\mathcal{R}_T = \sum \mathcal{R}_i^a + \sum \mathcal{R}_i^i + \mathcal{R}^c$ , the sum of all membrane-bound active ( $\mathcal{R}_i^a$ ) and inactive ( $\mathcal{R}_i^i$ ) Rac1 over all vertices ( $i = 1, \dots, N$ ), plus the amount uniformly dissolved in the cytosol ( $\mathcal{R}^c$ ). Then at each vertex on the membrane, we define the fractions  $R_i^a = \mathcal{R}_i^a / \mathcal{R}_T$  and  $R_i^i = \mathcal{R}_i^i / \mathcal{R}_T$ . For the cytosolic Rac1, the fraction is  $R^c = \mathcal{R}^c / \mathcal{R}_T$ . RhoA fractions are defined similarly, using the symbol  $\rho$  in place of  $R$ . These fractions are the dimensionless variables used in the kinetic model. To convert them into amount of the proteins, we need the total amount of Rac1  $\mathcal{R}_T$  and RhoA  $\rho_T$  in a cell. These values are estimated from the literature and given in Table 2 below.

In order to write reaction-diffusion equations (RDEs) for Rac1 and RhoA, we need to formulate the boundary diffusion fluxes for each. This requires converting the fractional amount on a vertex, say  $R_i^a$ , into a local concentration. As the total amount  $\mathcal{R}_T$  is constant, we can use the “fractional concentration” instead of the actual concentration in the RDEs. In our notation, the edge between vertices  $i$  and  $i + 1$  has a length  $l_i$ . Thus, vertex  $i$  is sandwiched by two edges of length  $l_{i-1}$  and  $l_i$ . As the amount of a GTPase, say  $R_i$ , is defined at each vertex, we calculate its “concentration” at the given vertex by spreading  $R_i$  over half of the two neighboring edges length  $L_i = (l_i + l_{i-1})/2$ . Now the diffusive flux from vertex  $i$  toward  $i + 1$  can be obtained from Fick’s law:

$$J_i = -D \frac{R_{i+1}/L_{i+1} - R_i/L_i}{l_i}. \quad (\text{S1})$$

---

\*Corresponding author. E-mail: james.feng@ubc.ca

The reaction-diffusion equations can thus be discretized using the net flux ( $J_{i-1} - J_i$ ) at this vertex. The fluxes can be written for all membrane-bound Rac1 and RhoA species in the same way. Recall that in the above,  $l_i$  and  $L_i$  may vary in time as the edges stretch and contract elastically.

The biochemical kinetics for Rac1 is described by the following reaction-diffusion equations:

$$\frac{dR_i^a}{dt} = K^+ R_i^i - K^- R_i^a + (J_{i-1}^a - J_i^a), \quad (\text{S2})$$

$$\frac{dR_i^i}{dt} = -K^+ R_i^i + K^- R_i^a + (J_{i-1}^i - J_i^i) + \frac{M^+ R^c}{N} - M^- R_i^i, \quad (\text{S3})$$

$$\frac{dR^c}{dt} = \sum_{i=1}^N \left( -\frac{M^+ R^c}{N} + M^- R_i^i \right), \quad (\text{S4})$$

where  $J_i^a$  and  $J_i^i$  are the membrane diffusive flux from vertex  $i$  to vertex  $i+1$  of active and inactive Rac1, respectively, approximated by using Fick's law with a membrane diffusivity  $D$ .  $K^\pm$  are the activation and deactivation rates for the membrane-bound Rac1, and  $M^\pm$  are the membrane association and dissociation rates of the inactive Rac1. Analogous equations are written for RhoA, with a similar set of rate parameters:

$$\frac{d\rho_i^a}{dt} = \kappa^+ \rho_i^i - \kappa^- \rho_i^a + (j_{i-1}^a - j_i^a), \quad (\text{S5})$$

$$\frac{d\rho_i^i}{dt} = -\kappa^+ \rho_i^i + \kappa^- \rho_i^a + (j_{i-1}^i - j_i^i) + \frac{\mu^+ \rho^c}{N} - \mu^- \rho_i^i, \quad (\text{S6})$$

$$\frac{d\rho^c}{dt} = \sum_{i=1}^N \left( -\frac{\mu^+ \rho^c}{N} + \mu^- \rho_i^i \right). \quad (\text{S7})$$

In all the results reported, we have used  $N = 16$  based on the ‘‘mesh-refinement’’ studies conducted by Merchant *et al.* [3]. In the polygonal representation of the cells, some of the parameter values depend on  $N$ . Should one choose to use a different  $N$ , these parameters will need to be adjusted accordingly. Such cases are noted in the following.

The reaction rates  $K^\pm$  and  $\rho^\pm$  in the RDEs are central to the kinetic model. It is through these rates that the nonlinear effect allowing for cell polarization enters, as do signals due to CIL, COA, tension mediated Rac1 inhibition, stochastic modulation of repolarization and the chemotactic gradient. These interactions are illustrated in the wiring diagram of Fig. S1.

- The Rac1 activation rate  $K^+(i, t)$ , at vertex  $i$  and time  $t$ , is the sum of a baseline rate  $K_b^+$  and an auto-activation rate  $K_A^+$ , each modulated by additional effects:

$$K^+(i, t) = [x_r(i, t) + x_a(i, t)]K_b^+ + \frac{[R_i^a/L_i(t)]^3}{C_H^3 + [R_i^a/L_i(t)]^3} K_A^+[1 + C_i(t)], \quad (\text{S8})$$

where  $x_r$  is the randomization factor and  $x_a$  is the co-attraction (COA) factor. Their time-dependence is understood but not always written out explicitly in the following. The auto-activation of Rac1 is represented by a Hill function with a half-max constant  $C_H$  [4], and amplified by a chemotactic factor  $(1 + C_i)$  that has been discussed in the main text (Eqs. 2–

4). The randomization factor allows the cell to periodically nucleate new Rac1 hotspots which may potentially mature and out-compete the existing protrusive front. Roughly every  $T_r$  minutes (sampled from a normal distribution with a mean of  $T_r$  and a standard deviation of  $0.1T_r$ ), we randomly select 25% of the vertices on a cell and set  $x_r = R$  on them for the duration until the next random selection, at which point  $R$  is put to 1 on those vertices that are not chosen again for the new cycle of upregulation. This produces the random Rac1 hotspots. A default value of  $R = 10$  is used in all results reported except for those in Fig. 4(b) and Fig. S7. Numerical experimentation shows that the model is not sensitive to the percentage 25%. It produces qualitatively the same outcome when the percentage changes from 6.25% to 50%, although for very low percentages a larger  $R$  value is needed. For all simulations we have used  $T_r = 40$  min. Together with the mechanical parameters of the model, the  $R$  and  $T_r$  values ensure that a single cell spends roughly 20 min each in its run and tumble phases [5]. The COA factor  $x_a(i)$  is calculated as follows. For cell  $a$ , we calculate the distance  $s_{ij}$  between its vertex  $i$  and vertex  $j$  on another cell  $b$ . Following Woods *et al.* [6], we assume an exponential decay of the C3a signal emitted from  $j$  such that vertex  $i$  on cell  $a$  receives a COA signal

$$\chi(i, j) = \frac{2^{-s_{ij}/l_c} M_{\text{COA}}}{(1 + y_{ij})^2}, \quad (\text{S9})$$

where  $l_c = 110 \mu\text{m}$  is the half-decay length [6] and  $M_{\text{COA}}$  is a dimensionless maximum COA strength. The denominator of Eq. (S9) is a ‘‘screening effect’’ due to cells intervening between vertices  $i$  and  $j$ ,  $y_{ij}$  being the number of times that the line connecting  $i$  and  $j$  passes through another cell other than  $a$  and  $b$ . Finally,  $x_a(i) = \sum_b \sum_{j=1}^N \chi(i, j)$  is computed by summing  $\chi(i, j)$  over all vertices of all the other cells.

As the COA factor  $x_a$  sums up influence from all other cells, it tends to be greater for larger clusters. To normalize the COA effect, we have tuned the maximum COA strength  $M_{\text{COA}}$  to achieve a mean cell-cell distance (between centroids) of 1.4–1.5 times its initial value. Among the results on cell clusters in the main article (Sec. 3.2 and Sec. 3.4 therein), the following values have been used for different cluster sizes:

$n$	2	4	9	16	25	36	49
$M_{\text{COA}}$	24	24	16	14	12	9	8

These values correspond to  $N = 16$  vertices on each cell. Should the number of vertices  $N$  change,  $M_{\text{COA}}$  is scaled by  $16/N$  so as to maintain the same level of COA effect regardless of the artificial resolution of membrane discretization.

- The Rac1 inactivation rate  $K^-(i, t)$  is the sum of a baseline rate  $K_b^-$  and a RhoA-mediated mutual inhibition rate  $K_{MI}^-$ , each modulated by additional effects:

$$K^-(i, t) = [x_s(t) + x_{\text{CIL}}(i, t)]K_b^- + \frac{[\rho_i^a/L_i(t)]^3}{C_H^3 + [\rho_i^a/L_i(t)]^3}K_{MI}^-, \quad (\text{S10})$$

where  $x_s$  is the tension-mediated Rac1 inhibition factor,  $x_{\text{CIL}}(i)$  is the CIL signal at vertex  $i$ . The RhoA inhibition of Rac1 is reflected by the factor in front of  $K_{MI}^-$ , which is a Hill function of the local active RhoA with a half-max constant  $C_H$ .

The tension-mediated Rac1 inhibition [7] is modelled as a Hill function of the strain of the entire cell circumference  $s$ , as the tension inhibition likely saturates at large tension or strain:

$$s = \frac{1}{Nl_0} \sum_{i=1}^N l_i - 1, \quad (\text{S11})$$

$$x_s = \max \left( M_s \frac{s^3}{s_H^3 + s^3}, 0 \right), \quad (\text{S12})$$

where  $l_0$  is the length of each edge of the undeformed cell,  $l_i$  is that of a deformed edge,  $s_H = 0.1$  is the half-max constant and  $M_s = 40$  is the maximum magnitude of strain mediated Rac1 inactivation. These values are chosen to produce a suitable level of tension-inhibition of Rac1. If the entire membrane is under compression,  $x_s$  is set to 0.

The CIL factor  $x_{\text{CIL}}(i)$  is activated if the straight-line distance  $d_i$  between vertex  $i$  and the closest edge or vertex on a neighboring cell falls below a threshold  $d_m$ . We define a truncated linear ‘‘CIL influence’’

$$x_c(i) = \begin{cases} 0, & d_i \geq d_m \\ M_{\text{CIL}}(1 - \frac{d_i}{d_m}), & d_i < d_m \end{cases}, \quad (\text{S13})$$

where  $M_{\text{CIL}}$  is the maximum magnitude of the CIL signal. Then  $x_{\text{CIL}}(i)$  is calculated from the average of the 3 neighboring vertices:

$$x_{\text{CIL}} = \frac{x_c(i-1) + x_c(i) + x_c(i+1)}{3}. \quad (\text{S14})$$

We have chosen  $d_m = 0.5 \mu\text{m}$  and  $M_{\text{CIL}} = 60$  for our membrane of  $N = 16$  vertices. If the number of vertices  $N$  should change,  $M_{\text{CIL}}$  changes as  $60 \times 16/N$  so as to maintain the same level of CIL effect regardless of the artificial resolution of membrane discretization.

Note that earlier work has demonstrated different CIL outcomes depending on whether two cells make head-to-head or head-to-tail collisions [8, 9]. As our model treats CIL through the same Rac/Rho dynamics as govern polarization, it can predict these outcomes without the need of postulating differing collision rules [10]. In particular, head-to-head collision leads to a prolonged contact that has a high probability of reversing the polarity of both cells. Head-to-tail contacts are typically short and rarely produce repolarization; the trailing cell pauses briefly and then resumes its moving toward the leader. These scenarios have been reported in Merchant *et al.* [3], Sec. 3.2 and Movies 3, 4 and 7. More recent experiments have suggested the possibility of site-dependent cell-cell contact [11, 12], which adds additional nuance to CIL. Essentially, polarization of Rho GTPases likely also causes polarization of cadherin and other membrane-bound proteins that affect CIL. As a result, different biochemistry may be

at work in head-head and head-tail contacts. Our current model does not account for such mechanisms.

- The RhoA activation rate  $\kappa^+$  consists of a baseline rate  $\kappa_b^+$  modulated by CIL and an auto-activation term modelled by a Hill function:

$$\kappa^+(i, t) = x_{\text{CIL}}(i, t)\kappa_b^+ + \frac{[\rho_i^a/L_i(t)]^3}{C_H^3 + [\rho_i^a/L_i(t)]^3}\kappa_A^+, \quad (\text{S15})$$

where  $x_{\text{CIL}}$  is the same as above, and  $C_H$  is the half-max constant for RhoA auto-activation.

- The RhoA inactivation rate  $\kappa^-$  consists of a baseline rate  $\kappa_b^-$  and a Rac1-mediated mutual inhibition effect modelled by a Hill function:

$$\kappa^-(i, t) = \kappa_b^- + \frac{[R_i^a/L_i(t)]^3}{C_H^3 + [R_i^a/L_i(t)]^3}\kappa_{MI}^-, \quad (\text{S16})$$

$C_H$  being the half-max constant in the Hill function.

- The membrane association and dissociation rates for Rac1 and RhoA,  $M^\pm$  and  $\mu^\pm$ , are constants given in Table 2. Since they multiply onto the local amount of the proteins to give their local rate of change, these constants do not vary with the edge length or  $N$ .

## 2 Mechanical model

The position and movement of our model cells are indicated by the position  $\mathbf{r}_i$  and velocity  $d\mathbf{r}_i/dt$  of its vertices. The motion of each vertex is determined by the total force on it through overdamped dynamics:

$$\eta \frac{d\mathbf{r}_i}{dt} = \mathbf{E}_{i-1} + \mathbf{E}_i + (p + F_i) \mathbf{n}_i, \quad (\text{S17})$$

where  $\eta$  is a friction factor due to, e.g., a viscous medium or adhesion to a substrate,  $\mathbf{E}_i$  is the elastic tension along the edge between vertices  $i$  and  $i + 1$ ,  $p$  is the homogeneous cytoplasmic pressure,  $F_i$  is the protrusive or retractive force on vertex  $i$ , and  $\mathbf{n}_i$  is the outward unit normal vector, which bisects the polygonal angle at that vertex (Fig. S2). The elastic tension obeys linear elasticity with modulus  $\lambda$  and an undeformed edge length  $l_0$ . Cytoplasmic pressure resists changes in a cell's area:

$$p = K_c \left[ 1 - \frac{A^c(t)}{A_0^c} \right], \quad (\text{S18})$$

where  $A^c(t)$  is the cell area at time  $t$ ,  $A_0^c$  is its resting area, and  $K_c$  is related to the bulk modulus of the cell. As we have found few relevant data in the literature, we have used a value of  $K_c = 625$  nN to keep the cell area change at about 5% on average. As the pressure force  $p$  is applied onto each vertex, the coefficient  $K_c$  should be varied according to  $625 \times 16/N$  nN if a different  $N$  is used.

Protrusive and contractile forces are proportional to the activity of Rho GTPase at a node. If the normalized activity of Rac1 is greater than that of RhoA at a vertex, the active force is

protrusive (positive). Otherwise it is contractile (negative):

$$F_i = \begin{cases} K_R \min(R_i^a - \rho_i^a, 0.05), & R_i^a > \rho_i^a \\ -K_\rho \min(\rho_i^a - R_i^a, 0.05), & R_i^a \leq \rho_i^a \end{cases}, \quad (\text{S19})$$

where  $K_R$  and  $K_\rho$  are constants governing the magnitude of the Rac1 and RhoA forces, respectively. Upon contact, CIL induces a transition from Rac dominance to Rho dominance in the region of contact. The resulting contractile forces typically cause the cells to withdraw from each other. Besides, we implement an exclusion rule to prevent overlap between neighboring cells. If over one time step  $\Delta t = 2$  s, a vertex would cross the boundary of another cell, we shorten the displacement of the intruding vertex so it ends up just outside the cell boundary. As we use overdamped mechanics, this position correction is tantamount to a repulsive force due to volume exclusion. Our model omits the detailed pathways leading from polarization of GTPases to the production of protrusion and contraction forces, e.g., via actomyosin assembly. Instead, we express these forces as truncated linear functions of the active Rac1 and RhoA levels at each vertex. Models for Rac-Rho competition, including our own, typically have regimes of bistability where either Rho or Rac dominates. We have chosen here to link the force of protrusion/contraction directly to that Rac-Rho balance, for simplicity.

The reason for implementing a cap to the linear dependence is as follows. Prass *et al.* [13] measured the protrusion forces at the forefront of lamellipodia by placing an atomic force microscopy (AFM) cantilever in the path of a migrating fish keratocyte. They obtained a stalling force around 1 nN, corresponding to about 100 polymerizing actin filaments pushing on every 1  $\mu\text{m}$  of the leading edge. The upper bound on this force may be due to a variety of constraints, e.g. limited space for a certain number of actin barbed ends and finite supply of any of the proteins regulating actin polymerization. Without further information, we have implemented an upper bound on  $R^a - \rho^a$  in our highly simplified expression above.

The threshold of 0.05 is inspired by the modeling of Jilkin *et al.* [4]. These authors inferred from experimental sources that a migrating cell should have about 40% of its GTPases in the membrane-bound activated state. In our notation, this corresponds to 2.5% on each of the  $N = 16$  vertices of our model membrane. Considering that only about half of the vertices will be inside the Rac1-rich protrusion front, the level of  $R^a$  on such a vertex should be on the order of 5%. This characteristic level is used, absent more pertinent data, as the threshold at which the upper bound for the forces is set.

### 3 Parameter Estimation

We divide the model parameters roughly into two categories: geometric and physical parameters, and biochemical parameters. Some of these parameters are varied in the study. But it is useful to establish a “standard” set of parameter values as the basis for such parametric variations. Such standard values are tabulated below for each of the two groups, with sources for the adopted values and additional explanations provided in footnotes.

Symbol	Description	Value	Sources
$d$	cell diameter	40 $\mu\text{m}$	[5]
$\eta$	viscous friction factor	290 $\text{nN s } \mu\text{m}^{-1}$	[14–16] <sup>1</sup>
$\lambda$	stiffness of cortex	80 $\text{nN } \mu\text{m}^{-1}$	[17, 18] <sup>2</sup>
$D$	membrane diffusivity	0.25 $\mu\text{m}^2 \text{ s}^{-1}$	[4, 19]
$K_R$	protrusive force constant	$\frac{0.3Nl_0}{0.4} \times 3 \text{ nN } \mu\text{m}^{-1}$	[13] <sup>3</sup>
$K_\rho$	contractile force constant	0.2 $K_R$	[13] <sup>4</sup>

Table 1: Geometric and physical parameters used in our model.

<sup>1</sup>Ref. [14] measured the viscosities of various embryonic tissue, and Refs. [15, 16] adapted these to 2D viscosities of 100–1000  $\text{nN s } \mu\text{m}^{-1}$ .

<sup>2</sup>We have converted the measured stiffness from 3D to 2D by multiplying it by a characteristic length of 10  $\mu\text{m}$ .

<sup>3</sup>The stalling force on actin filaments in lamellipodia is around 10 kPa [13]. Considering a lamellipodial height of 300 nm, we estimate a maximum protrusion force of  $3 \text{ nN } \mu\text{m}^{-1}$  on the membrane in our 2D model. Assuming a fraction (0.3) of the maximum force is achieved at a typical 40% whole-cell Rac1 activation level [4], we estimate the  $K_R$  coefficient for each of the  $N$  membrane vertices as the value shown.  $l_0 = d \sin(\pi/N)$  is the length of each of the  $N$  edges of the cell membrane, in units of  $\mu\text{m}$ , and  $N = 16$  is used in all the simulations reported.

<sup>4</sup>The contractile force constant  $K_\rho$  should be lower than the protrusive force constant  $K_R$  on account of adhesive frictions on the substrate. We have chosen the factor 0.2 such that protrusion/contraction forces on a single cell, coupled with the friction factor  $\eta$ , produce the correct single-cell speed.

Symbol	Description	Value	Sources
$C_H$	half-max constant in Hill function	$\frac{0.4}{Nl_0} \mu\text{m}^{-1}$	[4] <sup>5</sup>
$M^-, \mu^-$	Rac1, RhoA membrane dissociation rate	$0.15 \text{ s}^{-1}$	[20] <sup>6</sup>
$M^+, \mu^+$	Rac1, RhoA membrane association rate	$0.02 \text{ s}^{-1}$	[20]
$K_b^+$	baseline Rac1 activation rate	$2.4 \times 10^{-3} \text{ s}^{-1}$	[4, 21, 22] <sup>7</sup>
$\kappa_b^+$	baseline RhoA activation rate	$2.8 \times 10^{-3} \text{ s}^{-1}$	[4, 21, 22] <sup>7</sup>
$K_a^+$	maximum Rac1 auto-activation rate	$5 \times 10^{-2} \text{ s}^{-1}$	[4, 21, 22] <sup>7</sup>
$\kappa_a^+$	maximum RhoA auto-activation rate	$3.9 \times 10^{-2} \text{ s}^{-1}$	[4, 21, 22] <sup>7</sup>
$K_b^-$	baseline Rac1 deactivation rate	$8 \times 10^{-4} \text{ s}^{-1}$	[4, 21, 22] <sup>8</sup>
$\kappa_b^-$	baseline RhoA deactivation rate	$6 \times 10^{-3} \text{ s}^{-1}$	[4, 21, 22] <sup>9</sup>
$K_{\text{MI}}^-$	rate of Rac1 inhibition by RhoA	$0.4 \text{ s}^{-1}$	[4, 21, 22] <sup>8</sup>
$\kappa_{\text{MI}}^-$	rate of RhoA inhibition by Rac1	$4 \times 10^{-2} \text{ s}^{-1}$	[4, 21, 22] <sup>9</sup>
$\mathcal{R}_T$	total amount of Rac1 in a cell	$2.5 \times 10^6$	[4, 23] <sup>10</sup>
$\rho_T$	total amount of RhoA in a cell	$1 \times 10^6$	[4, 23] <sup>10</sup>
$M$	Maximum chemoattractant concentration	7.5	(this work) <sup>11</sup>

Table 2: Biochemical parameters used in our model.

Given the large number of kinetic parameters in Table 2, and the wide range of possible variations due to GAP stimulation [21], one wonders how sensitive the outcome of the model is to the choice of these parameters. These kinetic rates are not easily measurable, but the overall timescales and steady-state activity levels (relative to baseline) can sometimes be inferred. Note

<sup>5</sup>We assume half-max in the Hill function at a characteristic steady-state whole-cell activity of 40% [4]. As the membrane has  $N$  segments of length  $l_0 = d \sin(\pi/N)$ , the half-max concentration is computed as given. For lack of data that would distinguish the various auto-activations and mutual inhibitions, we have used the same  $C_H$  for all the Hill functions involved.

<sup>6</sup>This is the measured Rho GTPase-GDI binding rate. We assume that Rho GTPases will only dissociate from the membrane in their inactive form, and their subsequent binding with cytosolic GDIs is rapid [19, 24].

<sup>7</sup>Using purified proteins, Ref. [21] measured an intrinsic activation rate of  $1.5 \times 10^{-4} \text{ s}^{-1}$  for both Rac1 and RhoA, but reported that GEF stimulation could accelerate activation 5 to 1000 times. Using the lifespan of membrane-bound Rho GTPases, Refs. [4, 22] arrived at estimations comparable to that used here.

<sup>8</sup>Using purified proteins, Ref. [21] measured an intrinsic Rac1 deactivation rate of  $1.8 \times 10^{-4} \text{ s}^{-1}$ , but reported that GAP stimulation could accelerate deactivation 5 to 4000 times. Refs. [4, 22] used values comparable to ours.

<sup>9</sup>Using purified proteins, Ref. [21] measured an intrinsic RhoA deactivation rate of  $3.5 \times 10^{-4} \text{ s}^{-1}$ , but reported that GAP stimulation could accelerate deactivation 5 to 4000 times. Refs. [4, 22] used values comparable to ours.

<sup>10</sup>Our Rho GTPases are represented as fractions of the total Rac1  $\mathcal{R}_T$  and total RhoA  $\rho_T$ . These total numbers of proteins are required to convert our dimensionless results to actual concentrations. Ref. [4] used values for COS-1 cells, which are similar in size to *Xenopus* NCC cells (see Fig. 2 in [23]). In estimating the protein copy numbers, we have adopted an approximate Rho GTPase molecular weight of 21 kDa  $\approx 3.5 \times 10^{-11} \text{ ng}$  [4]. For CHO epithelial cells, Ref. [25] reported Rac1 and RhoA amounts that are higher by a factor of about 2.

<sup>11</sup>We have tested a range of  $M$  values from 0 to 10, with the baseline  $M = 7.5$  being a weak gradient to which a cluster responds in chemotaxis but a single cell hardly does.

that the mechanical parameters are not subject to the same degree of variability.

To address the uncertainty in the evaluation of the kinetic parameters, Merchant *et al.* [3] have carried out a comprehensive test of their model’s sensitivity to the kinetic parameters, varied typically over a 100-fold range (from 0.1 to 10 times the standard values). They have found that the 3 key features of the model prediction—cell polarization, COA and CIL—are largely robust over the ranges tested. Details of their parametric study can be found in the Supplemental Information of [3] (URL: <https://doi.org/10.1016/j.ydbio.2018.01.013>). Considering the similarity between our current kinetic model and the earlier one, we have not redone the parametric study here.

## 4 Quantifying Velocity Alignment

First, we determine the velocity vector of each cell by measuring its displacement over a prescribed time period  $\Delta t$ . We have tested  $\Delta t$  ranging from 5 min to 40 min, and the cross-correlation shows essentially the same trend, although somewhat larger values for longer  $\Delta t$ . This is understandable since a longer  $\Delta t$  overlooks short-lived meanderings of the cell and should yield a more directional velocity vector, and the neighbor-neighbor correlation should thus appear stronger. We have chosen to report data based on  $\Delta t = 5$  min.

At the end of each  $\Delta t$  period, we construct a snapshot of the velocity vectors for all  $N_c$  cells in a cluster. Then for each cell  $i$  with velocity vector  $\mathbf{v}_i$ , we calculate its instantaneous velocity correlation with its nearest  $N_n$  neighbors:

$$R_i = \frac{1}{N_n} \sum_{j=1}^{N_n} \frac{\mathbf{v}_i \cdot \mathbf{v}_j}{|\mathbf{v}_i||\mathbf{v}_j|}. \tag{S20}$$

We have tested several  $N_n$  values. Going from  $N_n = 4$  to 10, the final velocity correlation is slightly reduced for all clusters, but the same qualitative trend holds. This is reasonable as farther neighbors are not as well correlated as the nearest few. We have reported results for  $N_n = 4$  in Fig. 10 of the main paper and  $N_n = 10$  in Fig. S8 below.

Finally, the velocity cross-correlation  $R_v$  is computed from  $R_i$  through 3 levels of averaging. First we average  $R_i$  over all cells ( $i = 1, 2, \dots, N_c$ ) in the cluster at each time. Then we time-average over the duration of each simulation for the cluster. Finally we average over the 20 repeated realizations of the simulation.

## 5 Supplemental Figures

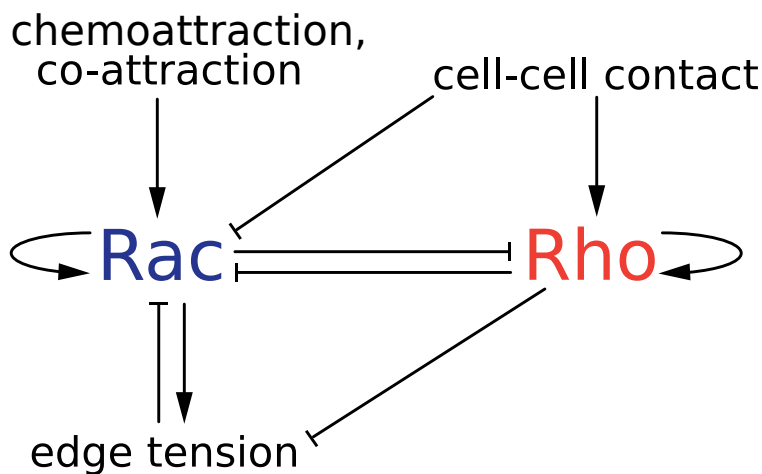


Figure S1: Wiring diagram for the autocatalysis and mutual inhibition of Rac1 and RhoA. These GTPases are also affected by edge tension, co-attraction, contact inhibition and the chemoattractant gradient.

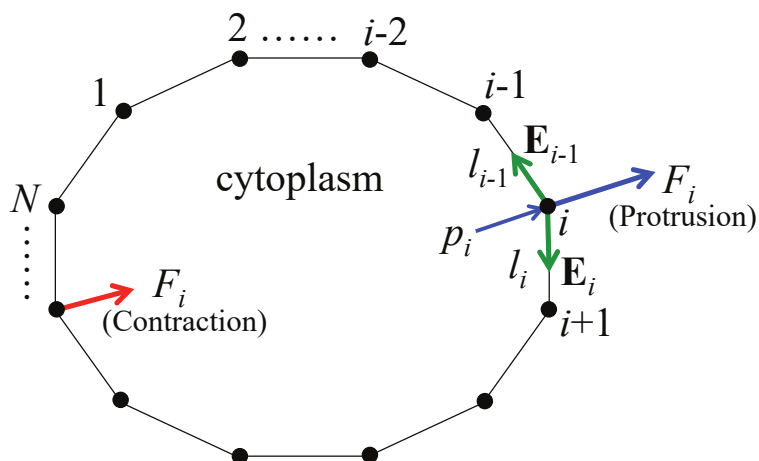


Figure S2: A model cell represented by a polygon of  $N$  vertices connected by elastic edges. The edge between vertices  $i$  and  $i + 1$  has length  $l_i$  and carries an elastic tension of  $\mathbf{E}_i$ . The normal forces include pressure  $p_i$  and a protrusion or contraction force  $F_i$ .

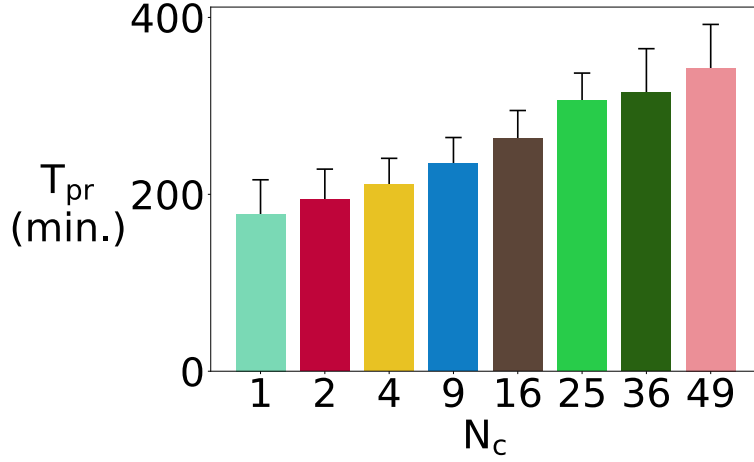


Figure S3: The protrusion lifetime  $T_{pr}$  increases with group size  $N_c$  in the absence of a chemoattractant ( $M = 0$ ). We define a protrusion as a vertex on which the active Rac1 exceeds 25% of the maximum among all vertices and this percentage exceeds that for active RhoA on that vertex.  $T_{pr}$  is computed by averaging the lifetime of all protrusions over the duration of each simulation, and then over the 20 realizations of the simulation. This provides additional support, alongside Fig. 3 of the main text, to the idea that a group of cells exhibits greater directional persistence even in the absence of a chemoattractant. We have used the standard set of parameters except  $M = 0$ .

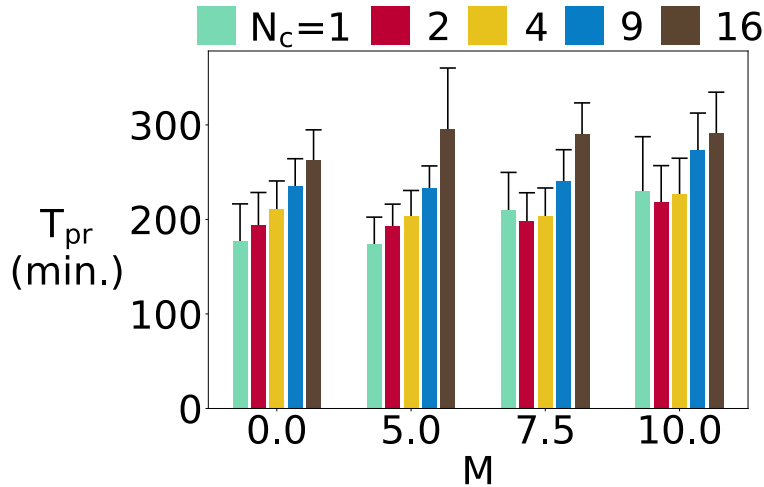


Figure S4: The averaged protrusion lifetime increases with cluster size during chemotaxis. Each group of bars are taken at a fixed magnitude of the chemoattractant gradient  $M$ . All other parameters are at their standard values.

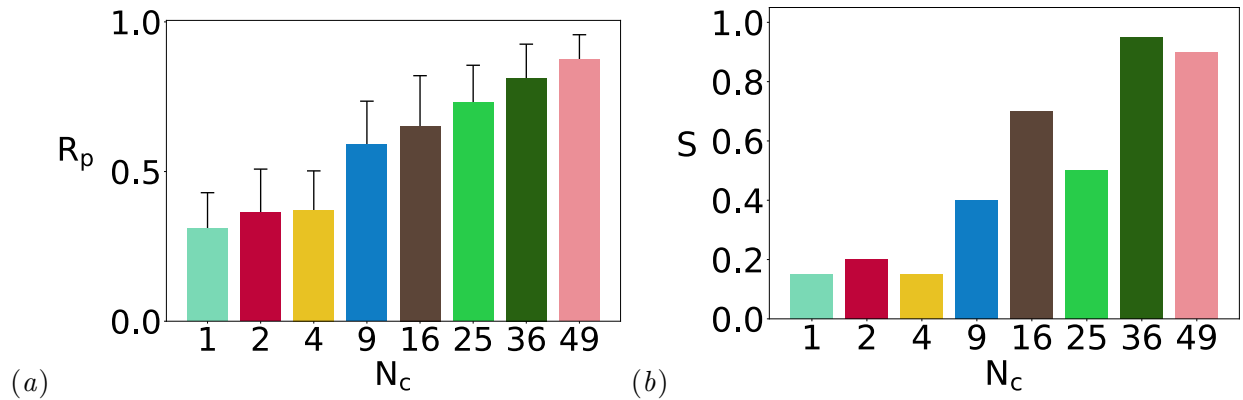


Figure S5: Group advantage in chemotaxis generally increases with the group size  $N_c$ , but appears to saturate for larger clusters. This is represented by (a) the cluster centroid persistence ratio  $R_p$ , and (b) the success rate  $S$ . We have used the standard set of parameters.

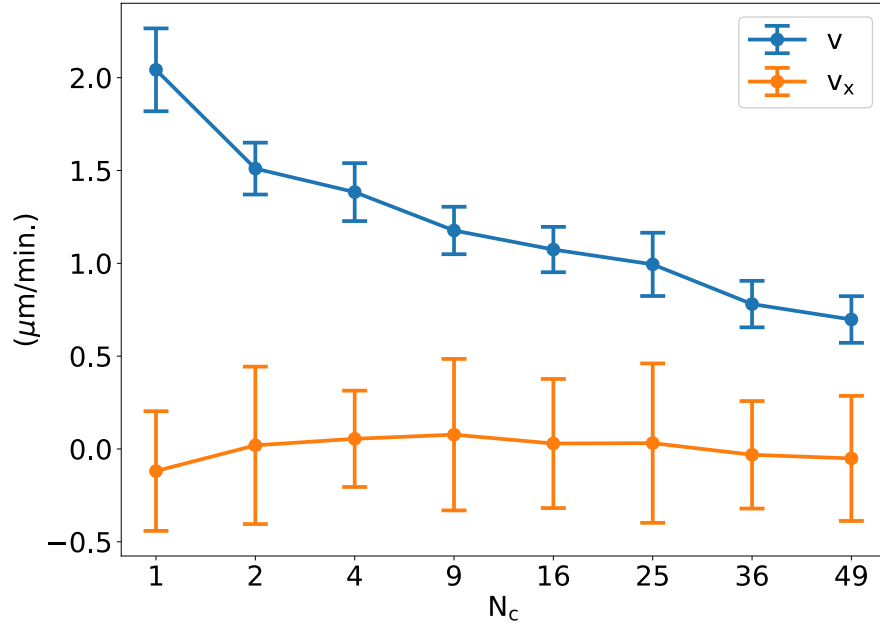


Figure S6: In the absence of chemoattractant ( $M = 0$ ), the cluster centroid shows no appreciable directional migration, as the  $x$  component of its centroid velocity essentially averages to zero. The centroid speed  $v$  decreases moderately with increasing cluster size.

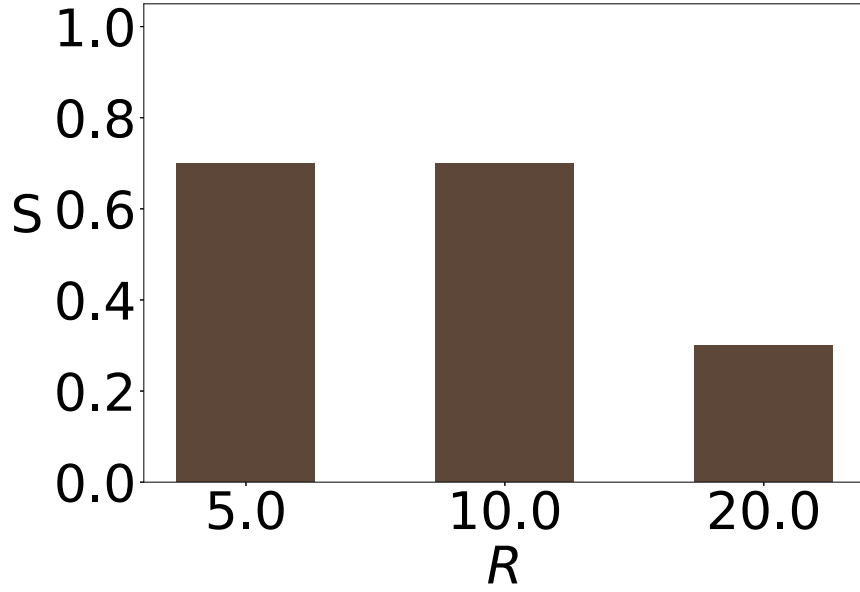


Figure S7: As the magnitude of the random noise  $R$  increases, the success ratio  $S$  of a group of 16 cells decreases. All other parameters are at their standard values.

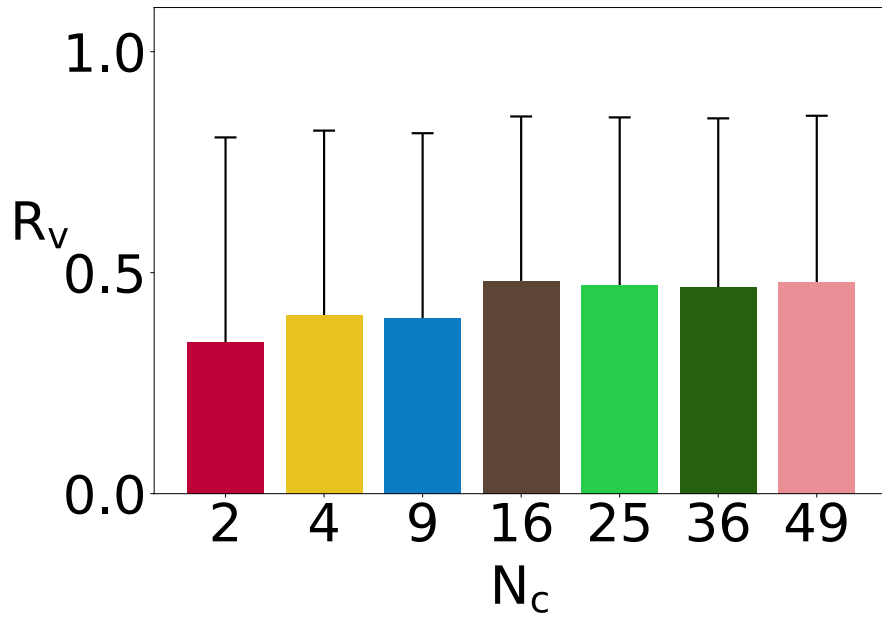


Figure S8: The cross-correlation  $R_v$  of the cell velocity vector computed by including 10 nearest neighbors in Eq. (S20).  $R_v$  increases with the cluster size  $N_c$  but saturates for larger clusters. This trend is the same as shown in Fig. 10 of the main paper, which plots  $R_v$  computed using 4 nearest neighbors.

## 6 Supplemental Movies

Eight supplemental movies can be downloaded from the article’s home page. Below are their captions.

Movie S1: A representative simulation of the run-and-tumble movement of a single cell in the absence of chemoattractant. The blue line segments pointing outward indicate the local active Rac1 level, while the red segments pointing inward the local active RhoA level. Over a long period, the trajectory resembles random walk. During the relatively straight segments of the trajectory (the “run” phase), the cell speed is around  $3 \mu\text{m}/\text{min}$ , and the run phase lasts about 20 min on average before the cell repolarizes and turns.

Movie S2: A representative simulation of the movement of a 16-cell cluster in the absence of chemoattractant. Compared with the single-cell behavior of Movie S1, the cluster’s centroid shows a stronger persistence in directional movement.

Movie S3: A representative simulation of a single cell chemotaxing successfully up a strong gradient ( $M = 10$ ). The green dot and circle to the right mark respectively the source of the chemoattractant and the “target zone”.

Movie S4: A representative simulation of a 16-cell cluster chemotaxing successfully up a relatively weak gradient  $M = 7.5$ .

Movie S5: A representative simulation of a solitary cell that fails to chemotax up the same gradient  $M = 7.5$  as in Movie S4, where the 16-cell cluster chemotaxes successfully.

Movie S6: Suppressing contact inhibition of locomotion (CIL) compromises the group advantage in chemotaxis for a 16-cell cluster. With  $M_{\text{CIL}}$  reduced from its standard value of 60 to 15, the cluster forms a close clump that fails to chemotax efficiently, in a scenario that resembles the experimental observation (Movie S8) of Theveneau *et al.* [5].

Movie S7: Suppressing co-attraction (COA) abolishes the group advantage in chemotaxis for a 16-cell cluster. With  $M_{\text{COA}}$  set to 0, the cluster scatters and fails to chemotax efficiently, in a scenario that resembles the experimental observation (Movie S6) of Carmona-Fontaine *et al.* [26].

Movie S8: Chemotaxis is lost for a 16-cell cluster when the magnitude of the random noise is doubled to  $R = 20$ . All other parameters are at their standard values.

## References

- [1] Y. Mori, A. Jilkinе, L. Edelstein-Keshet, Wave-pinning and cell polarity from a bistable reaction-diffusion system, *Biophys. J.* 94 (2008) 3684–3697.
- [2] W. R. Holmes, L. Edelstein-Keshet, Analysis of a minimal Rho-GTPase circuit regulating cell shape, *Phys. Biol.* 13 (2016) 046001.
- [3] B. Merchant, L. Edelstein-Keshet, J. J. Feng, A Rho-GTPase based model explains spontaneous collective migration of neural crest cell clusters, *Dev. Biol.* 444 (2018) S262–S273.
- [4] A. Jilkinе, A. F. Marée, L. Edelstein-Keshet, Mathematical model for spatial segregation of the Rho-family GTPases based on inhibitory crosstalk, *Bull. Math. Biol.* 69 (2007) 1943–1978.
- [5] E. Theveneau, L. Marchant, S. Kuriyama, M. Gull, B. Moepps, M. Parsons, R. Mayor, Collective chemotaxis requires contact-dependent cell polarity, *Dev. Cell* 19 (2010) 39–53.
- [6] M. L. Woods, C. Carmona-Fontaine, C. P. Barnes, I. D. Couzin, R. Mayor, K. M. Page, Directional collective cell migration emerges as a property of cell interactions, *PLoS One* 9 (2014) e104969.
- [7] A. R. Houk, A. Jilkinе, C. O. Mejean, R. Boltyskiy, E. R. Dufresne, S. B. Angenent, S. J. Altschuler, L. F. Wu, O. D. Weiner, Membrane tension maintains cell polarity by confining signals to the leading edge during neutrophil migration, *Cell* 148 (2012) 175–188.
- [8] R. A. Desai, S. B. Gopal, S. Chen, C. S. Chen, Contact inhibition of locomotion probabilities drive solitary versus collective cell migration, *J. R. Soc. Interface* 10 (88) (2013) 20130717.
- [9] D. A. Kulawiak, B. A. Camley, W.-J. Rappel, Modeling contact inhibition of locomotion of colliding cells migrating on micropatterned substrates, *PLoS Comput. Biol.* 12 (2016) e1005239.
- [10] M. George, F. Bullo, O. Campàs, Connecting individual to collective cell migration, *Sci. Rep.* 7 (2017) 9720.
- [11] D. Li, Y.-L. Wang, Coordination of cell migration mediated by site-dependent cell–cell contact, *Proc. Natl. Acad. Sci. U.S.A.* 115 (42) (2018) 10678–10683.
- [12] W. Pannekoek, J. de Rooij, M. Gloerich, Force transduction by cadherin adhesions in morphogenesis, *F1000Res.* 8 (1044).
- [13] M. Prass, K. Jacobson, A. Mogilner, M. Radmacher, Direct measurement of the lamellipodial protrusive force in a migrating cell, *J. Cell Biol.* 174 (2006) 767–772.
- [14] G. Forgacs, R. A. Foty, Y. Shafrir, M. S. Steinberg, Viscoelastic properties of living embryonic tissues: a quantitative study, *Biophys. J.* 74 (1998) 2227–2234.

- [15] T. Bittig, O. Wartlick, A. Kicheva, M. González-Gaitán, F. Jülicher, Dynamics of anisotropic tissue growth, *New J. Phys.* 10 (2008) 063001.
- [16] J. Solon, A. Kaya-Copur, J. Colombelli, D. Brunner, Pulsed forces timed by a ratchet-like mechanism drive directed tissue movement during dorsal closure, *Cell* 137 (2009) 1331–1342.
- [17] T. G. Kuznetsova, M. N. Starodubtseva, N. I. Yegorenkov, S. A. Chizhik, R. I. Zhdanov, Atomic force microscopy probing of cell elasticity, *Micron* 38 (2007) 824–833.
- [18] J. Solon, I. Levental, K. Sengupta, P. C. Georges, P. A. Janmey, Fibroblast adaptation and stiffness matching to soft elastic substrates, *Biophys. J.* 93 (2007) 4453–4461.
- [19] K. Moissoglu, B. M. Slepchenko, N. Meller, A. F. Horwitz, M. A. Schwartz, In vivo dynamics of Rac-membrane interactions, *Mol. Biol. Cell* 17 (2006) 2770–2779.
- [20] J. L. Johnson, J. W. Erickson, R. A. Cerione, New insights into how the Rho guanine nucleotide dissociation inhibitor regulates the interaction of Cdc42 with membranes, *J. Biol. Chem.* 284 (2009) 23860–23871.
- [21] B. Huang, M. Lu, M. K. Jolly, I. Tsarfaty, J. Onuchic, E. Ben-Jacob, The three-way switch operation of Rac1/RhoA GTPase-based circuit controlling amoeboid-hybrid-mesenchymal transition, *Sci. Rep.* 4 (2014) 6449.
- [22] W. R. Holmes, B. Lin, A. Levchenko, L. Edelstein-Keshet, Modelling cell polarization driven by synthetic spatially graded Rac activation, *PLoS Comput. Biol.* 8 (2012) e1002366.
- [23] D. Michaelson, J. Silletti, G. Murphy, P. D’Eustachio, M. Rush, M. R. Philips, Differential localization of Rho GTPases in live cells regulation by hypervariable regions and RhoGDI binding, *J. Cell Biol.* 152 (2001) 111–126.
- [24] S. Das, T. Yin, Q. Yang, J. Zhang, Y. I. Wu, J. Yu, Single-molecule tracking of small GTPase Rac1 uncovers spatial regulation of membrane translocation and mechanism for polarized signaling, *Proc. Natl. Acad. Sci. U.S.A.* 112 (2015) E267–E276.
- [25] R. Krall, J. Sun, K. J. Pederson, J. T. Barbieri, In vivo Rho GTPase-activating protein activity of *pseudomonas aeruginosa* cytotoxin ExoS, *Infect. Immun.* 70 (2002) 360–367.
- [26] C. Carmona-Fontaine, E. Theveneau, A. Tzekou, M. Tada, M. Woods, K. M. Page, M. Parsons, J. D. Lambris, R. Mayor, Complement fragment c3a controls mutual cell attraction during collective cell migration, *Dev. Cell* 21 (2011) 1026–1037.